Spring 1-1-2017

Understanding the Variability in Thermospheric Nitric Oxide Flux Using Empirical Orthogonal Functions (EOFs)

Sierra Mae Flynn
University of Colorado Boulder, sierra.mae.flynn@gmail.com

Understanding the Variability in Thermospheric Nitric Oxide Flux using Empirical Orthogonal Functions (EOFs)

By

Sierra Mae Flynn

B.A., Astrophysics, University of Colorado at Boulder, 2015

B.S., Computer Science, University of Colorado at Boulder, 2015

M.S., Aerospace Engineering, University of Colorado at Boulder, 2017

A thesis submitted to the Faculty of the Graduate School of the University of Colorado in partial fulfillment of the requirement for the degree of Masters of Science

Department of Ann and H.J. Smead Aerospace Engineering Sciences

2017

This thesis entitled:
Understanding the Variability in Thermospheric Nitric Oxide Flux
using Empirical Orthogonal Functions (EOFs)
written by Sierra Mae Flynn
has been approved for the Department of Ann and H.J. Smead Aerospace Engineering Sciences

_____
Tomoko Matsuo (Committee chair)

_____
Delores Knipp (Committee member)

_____
Xinlin Li (Committee member)

Date _____

The final copy of this thesis has been examined by the signatories, and we find that both the content and the form meet acceptable presentation standards of scholarly work in the above-mentioned discipline.

Abstract

Flynn, Sierra Mae (M.S., Department of Ann and H.J. Smead Aerospace Engineering Sciences)

Understanding the Variability in Thermospheric Nitric Oxide Flux using Empirical Orthogonal Functions (EOFs)

Thesis directed by Professor Tomoko Matsuo

Quantifying the spatial and temporal variability of nitric oxide (NO) emissions in the thermosphere using eigenmodes will increase the understanding of how upper atmospheric NO behaves, and could be used to increase the accuracy of future space weather and climate models. NO flux (NOF) from 100-250 km altitude taken from 13 years of data observed by the SABER instrument onboard the TIMED satellite is decomposed into four empirical orthogonal functions (EOFs) and their amplitudes to: 1) determine the strongest modes of NO flux variability (NOFV) in the data set, and 2) develop a compact model of NOF. The first four EOFs account for 83% of the variability in the data. Their uncertainty is verified using cross-validation analysis. The first EOF represents 69% of the total variance and correlates strongly with Kp and XUV flux, suggesting that geomagnetic activity and solar weather account for a large portion of NOFV. EOF 2 shows annual and seasonal variations, possibly due to annual and seasonal thermospheric composition and temperature changes, and may represent the chemical "breathing mode" of NOFV. EOF 3 shows annual variations and correlates with energetic proton flux, and is strongest after solar energetic particle events (SEPs) and X-flares. EOF 3 may represent winter time SEP-enhanced diurnal tide effects. EOF 4 suggests a transport mechanism toward the poles and

outwards at the pre-dawn and post-dusk equator after strong storms. The NOF model is illustrated and the geophysical associations of the EOFs are discussed.

Acknowledgements

This project was partially funded by NASA grant NNX14AI17G and by AFOSR grant FA9550-17-1-0258.

I would like to thank my advisors and mentors Dr. Tomoko Matsuo and Dr. Delores Knipp for their endless support, insight, and enthusiasm for this thesis work. I additionally want to thank Dr. Xinlin Li for joining the thesis committee and providing feedback, and Dr. Martin Mlynczak for his encouragement and insight. Thank you to all the supportive professors, researchers, students, friends, and family that have encouraged me throughout my thesis work.

Additionally, I want to thank specific colleagues and contributors, including Liam Kilcommons, who has provided several data sets and information on the SABER NOF data set; Tristan Isaacs, whose presentations and results from his CU SPUR work has provided a solid basis for understanding the NOF chemistry; and Alfredo (Freddy) Cruz, who provided the SABER NOF data set and superposed epoch analysis code snippets.

The EOF maps presented here and preliminary interpretations were previously presented through Sierra Flynn's student poster ("Understanding the variability in thermospheric nitric oxide flux using empirical orthogonal functions (EOFs)") and a presentation ("Empirical Orthogonal Function (EOF) Analysis & Nitric Oxide Flux") at the Coupling, Energetics, and Dynamics of Atmospheric Regions (CEDAR) conference, June 18 – 23, 2017, Keystone, CO. The poster and presentation can be viewed online on the CEDAR wiki page.

Contents

List of Tables

List of Figures

Chapter I

Introduction

Nitric Oxide (NO) makes up a small percentage of the thermosphere's composition, but it is the most significant constituent in cooling the lower thermosphere (Bailey et al., 2004; Mlynczak et al., 2005). Thermospheric NO is produced and destroyed by auroral and solar drivers, via chemical reactions driven by photoelectrons, auroral electrons, and photodissociation (Barth et al., 2003; Cravens & Killeen, 1988; Solomon et al., 1999; Venkataramani et al., 2016). Thermal interactions associated with auroral Joule heating maintain NO in a vibrationally-excited state, during which it can emit in the infrared (IR) at 5.3 μm (Barth et al., 2009; Lu et al., 2010). The thermosphere is optically thin to this NO flux (NOF) IR radiation, which escapes the thermosphere completely, cooling it; half is radiated into space, and half into the lower atmosphere (Mlynczak et al., 2005). Although increased solar activity tends to heat and expand the atmosphere, Mlynczak et al. (2005) describe NO as a "natural thermostat" in recovering the thermosphere after a solar or geomagnetic storm. It has been shown that large solar storms are associated with such a significant increase in NOF that the thermosphere is cooled down below pre-storm levels (Lei et al., 2011, 2012). Knipp et al. (2013, 2017) noted that significant NO cooling tends to develop after the onset of shock-driven storms. Understanding how NOF responds to varying solar flux, as well as geomagnetic and solar storms, will help us understand how the thermosphere as a whole responds to these events.

Marsh et al. (2004) analyzed spatial and temporal variability of Student Nitric Oxide Experiment (SNOE) thermospheric NO density data between March 1998 and September 2000

using empirical orthogonal function (EOF) analysis. Their EOFs are estimated from the eigenvalue decomposition sample covariance, which range in altitude from 97.5 to 150 km and ±85° MLAT (geomagnetic latitude). Their EOFs are constrained to within 30 minutes of 10:45 local time. They found that over 85% of the total variability in the dataset could be described by 5 EOFs and their time-varying amplitudes. Performing correlation analysis on these EOFs revealed a strong correlation with Kp, solar declination, and F10.7 radio flux. This implied that NO density variability is strongly associated with geomagnetic storms and auroral forcing, day of year, and solar soft X-ray flux.

The Sounding of the Atmosphere using Broadband Emission Radiometry (SABER) instrument on NASA's TIMED (Thermosphere Ionosphere Mesosphere Energetics Dynamics) satellite, launched in 2001, continues this exploration of thermospheric nitric oxide. SABER is an atmospheric limb-scanning radiometer that measures the flux (in W/m^2) of NO emissions at 5.3 μm, which has been integrated from 100-250 km altitude from 2002 through 2015 (Mlynczak et al., 2003; Yee et al., 2003). The atmosphere is well sampled except near local solar noon. With the SABER NOF data set, we can expand upon the current knowledge of thermospheric NO and characterize its emissions. Motivation for this work stems from the need to characterize "global radiated power calculations that require consideration of the variation of NO emission" (Mlynczak et al., 2003). In this work, SABER NOF is decomposed into EOFs, deciphering the geomagnetic latitude and local-time dependence of height-integrated NOF for the first time. These EOFs provide us with nearly global coverage of NOF in geomagnetic coordinates. This data mining technique condenses the data and reduces noise, allowing for more efficient data assimilation, such as correlation analysis and predictive modeling of nitric oxide flux.

In addition to presenting these EOFs, the different processes that may influence NOF variability are explored. This is done using correlation analysis with geophysical processes, such as geomagnetic storm indices and solar flux, as well as using wavelet frequency decomposition to determine any periodic patterns in the EOFs. Superposed epoch analysis of the EOF amplitudes and reorthogonalization of EOFs around certain events support the geophysical interpretations. Additionally, exploring the variability and spatial distribution of NO can be applied to numerous research areas, including thermospheric characterization, satellite drag models, climate variability, atmospheric transport mechanisms, thermospheric tides, and ozone loss.

Arrangement of the Thesis

This paper is organized as follows: in Chapter II, the chemistry behind NO production, emissions, and destruction, as well as the geophysical relationships are reviewed from the literature. In Chapter III, the statistical techniques used are described, including EOF analysis, EOF reorthogonalization, correlation analysis, and wavelet decomposition. The SABER data and processing procedures are described in Chapter IV. In Chapter V, the EOF results and geophysical interpretations are presented, and in Chapter VI further potential geophysical contributions are discussed. EOF validation, model limitation, sources of error, and model performance are detailed in Chapter VII. Lastly, potential future work that can be done using this NOF EOF model is explored in Chapter VIII before presenting the conclusion in Chapter IX.

Chapter II

Background

Bailey et al. (2004) and Mlynczak et al. (2003) walk through the most significant production, emission, and destruction mechanisms of NO in the thermosphere:

Production: Before NO can be produced, molecular nitrogen is broken up into nitrogen atoms, some fraction of which are in an excited state, via a collision with a precipitating auroral electron or soft solar X-ray photoelectron (Equation 1) (Barth et al., 2003). Then, molecular oxygen reacts with atomic nitrogen to produce NO (Equation 2a and 2b). Equation 2a is the primary mechanism by which NO is produced below 110 km, and equation 2b gives the dominant source of NO above 110 km (Bailey et al., 2004; Jones, 2016; Richards, 2004). These reactions are highly temperature dependent (Richards, 2004).

$$e^* + N_2 \rightarrow N(^2D) + N + e^* \qquad (1)$$

$$N(^2D) + O_2 \rightarrow NO + O + h\nu_{5.3\mu m} \qquad (2a)^1$$

$$N(^4S) + O_2 \rightarrow NO + O + h\nu_{5.3\mu m} \qquad (2b)^1$$

Emission: NO may emit at 5.3 μm (infrared) from its ground-state vibration-rotation bands (Dalgarno, 1963; Kockarts, 1980; Mlynczak et al., 2003; Ogawa, 1976). NO may collide with atomic oxygen or an energetic electron (Equations 3a and 3b) after production, causing it to vibrationally excite and create NO flux (NOF) (Mlynczak et al., 2003). NO generated via Equations 2a and 2b may also be created with the vibrational energy necessary to radiate in the

[1] Emissions at values other than 5.3 μm are also possible. Since the SABER NO flux data set only consists of the 5.3 μm NO emissions, which are the dominant source of radiative cooling from 120-200 km (Venkataramani et al., 2016), it is emphasized here.

IR. The subsequent enhanced storm time NO cooling may last for a few days (Maeda et al. 1989, 1992; Mlynczak et al., 2003). Although maximum NO density occurs near 110 km, NO emissions peak at 130 km (Bailey et al., 2004; Mlynczak et al., 2003). Both the production and emission mechanisms are enhanced through Joule heating and during storm time (Mlynczak et al., 2003).

$$NO + O^* \rightarrow NO + O + h\nu_{5.3\mu m} \qquad (3a)^1$$

$$NO + e^* \rightarrow NO + e + h\nu_{5.3\mu m} \qquad (3b)^1$$

Destruction: NO can be destroyed in two ways: primarily via ground-state atomic nitrogen at all altitudes (Equation 4), or via a UV photon (Equation 5) (Richards, 2004). Both reactions are highly dependent on solar flux: the large amount of $N(^4S)$ produced by the Sun removes NO in Equation 4, and solar FUV radiation can also destroy it in Equation 5 (Richards, 2004). Although NO is primarily produced at night, it emits and dissociates when it is rotated into sunlight (Solomon et al., 1999). Once produced, NO remains in the thermosphere for about a day, but may remain longer when not exposed to solar radiation (i.e. during the high-latitude winter months) (Bailey et al., 2004). During these times, NO is transported down to the mesosphere at 70 km (Bailey et al., 2004). Bailey et al. (2004) also showed that NO is transported equatorward by winds during the winter. Richards (2004) argued that this transport must be at altitudes close to 110 km.

$$NO + N(^4S) \rightarrow N_2 + O \qquad (4)$$

$$NO + h\nu_{UV} \rightarrow N(^4S) + O \qquad (5)$$

NO production and flux variability have been tied with several geophysical and solar drivers, some of which are periodic. These include NO densities (Barth et al., 2009; Ridley et al., 1999), geomagnetic activity and Joule heating (Barth, 2010; Barth et al., 2009; Lu et al., 2010; Marsh et al., 2004; Richards, 2004; Weimer et al., 2015), solar flux and solar activity (Barth et al., 2009; Knipp et al., 2017; Marsh et al., 2004; Mlynczak et al., 2003; Solomon et al., 2012), thermospheric temperature (Mlynczak et al., 2003, 2005), thermospheric winds, tides, and gravity waves (Barth et al., 2009; Chang et al., 2016; Jones et al., 2016; Oberheide et al., 2013), and molecular and eddy diffusion (Cravens & Killeen, 1988; Richards, 2004). These geophysical associations with NO production and emission are explored in the NOF EOF results and discussions in Chapters 5 and 6.

Chapter III

Methods

The sparsity of the SABER data set makes it challenging to apply a conventional EOF analysis approach that relies on the eigenvalue decomposition of a sample covariance estimated from data with complete coverage. Instead, the sequential nonlinear regression method developed by Matsuo et al. (2002) is used to characterize dominant spatial modes of variability in the NOF data set as EOFs, which can be scaled by a time-varying scalar amplitude to represent the temporal variation. The variance of the time-varying amplitudes corresponds to the eigenvalues, while the eigenfunctions (or eigenmodes), as determined empirically from the data, are referred to as EOFs (or principal components). EOFs are by definition statistically independent, but several geophysical processes may contribute to the variability of an EOF, as discussed later. EOFs will be used as:

1. A low dimensional model of NOF spatiotemporal variability
2. A tool to understand how geophysical processes influence NOF variability
3. A data compression technique

An *i*th EOF $\Psi_i(\theta, \varphi)$ is a function of co-latitude $\theta = [0, \pi]$ and local time location (00:00 to 24:00 MLT) expressed in terms of radians, $\varphi = [0, 2\pi]$, defined in geomagnetic coordinates. This coordinate system was chosen since NO production, emission, and destruction depend on geomagnetic and solar forces. The EOF's signed time-varying amplitude is given by $\alpha_i(t)$. Based on the same approach described by Matsuo and Forbes (2010), the SABER residual NOF (the value after the mean is subtracted) y' at a given location and time (θ, φ, t) can be projected onto the principal subspace spanned by the leading n EOFs as:

$$\boldsymbol{y}' \approx \boldsymbol{\Psi\alpha} = \sum_{i=1}^{n} \alpha_i(t)\Psi_i(\theta,\varphi) = \sum_{i=1}^{n} \alpha_i(t) \sum_{k=1}^{K} \beta_k^{(i)} \Phi_k(\theta,\varphi) = \alpha_1(t)\boldsymbol{\Phi}(\theta,\varphi)\boldsymbol{\beta}^{(1)} + \cdots + \alpha_n(t)\boldsymbol{\Phi}(\theta,\varphi)\boldsymbol{\beta}^{(n)} \quad (6)$$

Where EOF $\Psi_i(\theta, \varphi)$ is expressed in terms of spherical harmonics Φ_k evaluated at location (θ, φ) and its coefficients $\beta_k^{(i)}$. The first $K = 64$ real spherical harmonics (with the integer degree $l = 0, \ldots, 7$ and the integer order $m = -l, \ldots, l$) are used in this study (see Appendix A for a mathematical description of the spherical harmonics). This provides a resolution of up to 24° (or 1.6 hours) for each set of spherical harmonics. Each EOF is a linear combination of these 64 spherical harmonics $\{\Phi_k(\theta, \varphi)\}$ scaled by $\beta_k^{(i)}$. The temporal resolution of $\alpha_i(t)$ is one orbit (96.8 minutes).

As for a conventional EOF method, the objective of the sequential nonlinear regression analysis of Matsuo et al. (2002) is to find a low-dimensional space that accounts for a large portion of the observed variance in a data set. After $\{\beta_k^{(1)}\}$ and $\alpha_1(t)$ are determined by iterative nonlinear regression, the projection onto the first EOF is subtracted from the SABER residual NOF to form the subsequent residual data. The QR method (i.e., Gram-Schmidt method) is then used to obtain orthogonal directions to $\{\beta_k^{(1)}\}$ in order to estimate $\{\beta_k^{(2)}\}$ and $\alpha_2(t)$ from the subsequent residual data. These steps are repeated for the first 7 EOFs, the first 4 of which are considered in this paper. In this analysis, the first 4 EOFs account for 83% of the total variance. See Appendix A for a detailed mathematical description of this method.

The 13 years of SABER NOF data has been condensed into a data set that is just 5.8% of its original size by accounting for a large amount of the variance in the SABER residual NOF using EOFs. By decomposing the data set this way, noise and data spikes are filtered out as well.

The resulting EOF maps have lower spatial and temporal resolution than the original data set, but they can be sampled at any location and time and return an interpolated value.

This EOF analysis has several drawbacks, and the uncertainty of the resulting EOFs needs to be carefully considered. In addition to the errors originating from instrument noise and pre-processing errors (e.g., those discussed in Mlynczak et al., 2003), this low-dimensional modeling has errors associated with the sequential regression and truncation techniques used to obtain the EOFs from the sparse data. A better fit could be obtained by increasing the number of spherical harmonics or increasing the number of EOFs in the fit, at the expense of overfitting and reducing effectiveness as a dimensional reduction tool, as discussed later.

EOFs are orthogonal and linearly independent, and therefore EOF coefficients are statistically uncorrelated in the principal subspace spanned by EOFs (Hartmann, 2016). It is tempting to try and directly associate each EOF with an independent geophysical process, but this cannot be guaranteed. However, correlation analysis can be performed on the EOF amplitudes and suspected drivers of the NOF variability (such as Kp index and solar flux). The degree of correlation and time-lag for these geophysical processes provides evidence for the driving factors of NOF production. Additionally, wavelet decomposition of the EOF amplitudes can reveal periodic signals and how they change over time. Publicly available geophysical databases and MATLAB's *crosscor* function and *cwt* function with the morse wavelet option are utilized to perform this analysis. Superposed epoch analysis (SEA), which averages each EOF amplitude for certain events (or epochs) over several days, provides a preliminary understanding of the mean EOF behavior for certain events over time. Lastly, reorthogonalization of EOFs around certain geophysical events helps support the geophysical interpretation of the EOFs. Reorthogonalization involves extracting the EOF amplitudes surrounding certain events (such as

coronal mass ejections (CMEs)), finding the eigenvectors and eigenvalues from the covariance of the EOF amplitudes, and projecting the original EOFs onto these eigenvectors. This produces a new set of EOFs that are more relevant to the certain geophysical events of interest.

Chapter IV

Data Description & Preparation

The nitric oxide flux data used in this analysis was obtained from the SABER instrument on NASA's TIMED satellite, which may be derived directly from standard SABER data products available on the SABER data website. Universal time, geographic latitude, geographic longitude, and NOF are acquired approximately every minute from 2002 through 2015, producing about 6.7 million data points.

To produce stationary EOFs, the data were first transformed to geomagnetic coordinates using the altitude-adjusted corrected geomagnetic coordinates system Python package (AACGMv2) at 130 km, the altitude of peak NO emissions (Mlynczak et al., 2003). The TIMED satellite is in a nearly-circular low Earth orbit with an inclination of 74.1 degrees and an altitude of 625 km. This inclination produces a rate of precession of about 2 degrees per day, or about two full precessions in inertial space per year, giving a solar time sampling period of about 61 days (Flynn, 2016). Consequently, TIMED performs a yaw maneuver every 61 days to prevent SABER from pointing into the Sun, producing few observations near local noon. This orbit also limits the scans to a geographic latitude range of -53°S to +85°N in the northern hemisphere, and +53°N to -85°S in the southern hemisphere, varying every 61 days. The resulting data distribution in 24° bins in geomagnetic coordinates is displayed in Figure 1 (note that 24° is one half the wavelength of a degree 7 spherical harmonic, which represents the highest resolution of EOF presented here). Although SABER does not scan above ±85° geographic latitude and avoids local noon, when converted to geomagnetic latitude and magnetic local time, SABER provides

nearly-global geomagnetic coverage. The apparent reduction in data at the equator occurs because AACGM coordinates are undefined there.

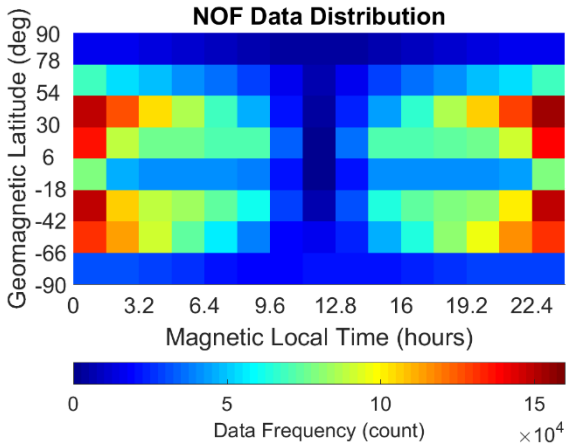

Figure 1: SABER's nitric oxide flux data distribution in geomagnetic coordinates, binned by geomagnetic latitude in 24˚ bins (1/2 the wavelength of a degree 7 spherical harmonic) and magnetic local time (MLT) in 1.6-hour (24˚) bins. The color bar resolution is 2,500 data points. The smallest bin centered at -6±12° MLAT, 12±0.8 MLT contains 576 data points.

Online databases were scouted for various geophysical data in order to perform correlation analysis on the NOF EOFs. Hourly proton flux, solar wind parameters, electric field strength, and magnetic field strength were obtained from OMNIWeb Plus, an online database containing hourly-averaged data taken by various missions. Daily FUV, MUV, and XUV were downloaded from LASP's SORCE mission website. Daily Dst, particle data (various proton and electron fluxes), solar data (F10.7), and geomagnetic data (Kp index every 3 hours) were obtained from NOAA. Daily UV data from TIMED SEE acquired through LASP's SEE website were also used. A list of coronal mass ejections (CMEs) observed by the DREAMS team was obtained from the University of Science and Technology of China DREAMS Wind ICME website. The high speed stream events (HSSs) analyzed were provided by McGranaghan et al. (2014). Sudden commencements were obtained from Observatori de l'Ebre at Ramon Llull University. A list of solar energetic particle events (SEPs) were acquired from NOAA SWPC

webpages. These data sets provided significant coverage in the time range of interest (2002-2015).

Chapter V

Results & Interpretation

Nitric Oxide Flux EOFs

The global NOF mean field (Figure 2) and the first four spatial modes of variability, or EOFs (Figure 3a-d) are obtained after applying the statistical methods to the SABER NOF data set as described in Chapter 3. The EOFs represent static patterns in space. The EOFs are unitless and normalized such that 0 (green) corresponds to no variability in that region. The signs of the EOFs are arbitrary until they are associated with their corresponding signed amplitudes in time, not shown here. These first 4 EOFs account for 83% of the total variability in the data set, as summarized in Table 1. The tapering of the percent variability explained by each consecutive EOF is revealed by EOFs 5, 6, and 7, thus given their small contributions to the total variability, they will not be discussed any further in this work.

	EOF 1	EOF 2	EOF 3	EOF 4	EOF 5	EOF 6	EOF 7
% Variability Explained	69.24	7.12	4.23	2.64	2.03	1.52	1.36
% Cumulative Variability	69.24	76.36	80.58	**83.22**	85.26	86.78	88.14
% Change	69.24	62.12	2.89	1.59	0.61	0.51	0.16

Table 1: Percent of variability explained by the first 7 EOFs.

Correlation analysis was performed on each EOF amplitude. A variety of 30 different solar, auroral, and geomagnetic drivers were tested. The 13 most relevant results are organized by absolute magnitude in Figure 3e-h. Additionally, periodic signals were detected using wavelet-based frequency analysis, shown in Figure 3i-l.

The EOF results displayed here, along with their correlations, lags, and wavelet decomposition, reveal significant implications about the geophysical association of these EOFs.

The strongest correlations in the data set are comparable to those of Weimer et al. (2015), who found that SABER NOF correlated strongly with a variety of geophysical parameters, including Kp, F10.7, MUV, XUV, Dst, IMF, solar wind speed, electric field, soft X-rays, sunspots, Poynting flux, thermospheric temperature, and Lyman-alpha solar radiation. It is important to note that although the EOFs presented here have high correlations with many geophysical parameters, they are not necessarily "driven" by one parameter over another. That is, EOF analysis cannot directly link EOFs with independent geophysical drivers (Björnsson & Venegas, 1997). The interpretation of the EOFs includes results from previous research to explain spatial structures and temporal behavior. In many cases correlations and lags also bolster the arguments made. In the subsequent sections, the mean NOF field and the EOFs are interpreted. Further discussion of these in terms of the relevant literature is held in Chapter 6.

Mean NOF Field

The NO mean field (Figure 2), shown in geomagnetic latitude and magnetic local time, is static in the spatial and temporal domains, and represents an average 5.3 μm NOF integrated from 100-250 km altitude in units of W/m^2. It shows significant NOF poleward of ±60° MLAT. This aspect of the mean field is consistent with NO densities derived from global Atmosphere Explorer-C (AE-C) NO UV emission maps in Cravens and Stuart (1978) and SNOE observational profiles in Barth et al. (2004). The pattern is likely a local-time realization of the zonal mean NO density patterns shown in Barth (1992, 1995), Barth et al. (2003, 2004), Solomon et al. (1999), and the Michelson Interferometer for Passive Atmospheric Spectroscopy (MIPAS) NO volume mixing ratio of Bermejo-Pantaleón et al. (2011). The dayside extension to sub-auroral regions is consistent with equatorward transport of aurorally-produced NO (Barth et al., 2003). The expansion of the daytime auroral oval enhancement is consistent with the NO

density spatial distributions presented in previous research (Marsh et al., 2004). Although some of this NO will be eliminated by photolysis after sunrise, a fraction remains to interact with the heated constituents of the dayside atmosphere. There is a small north-south asymmetry of the mean NOF that also appears in the SNOE NO density profiles of Marsh et al. (2004).

At 14 MLT, the NOF peaks along all geomagnetic latitudes. This broad-latitude post-noon emission is generally consistent with the temperature maximum in the post-noon Mass Spectrometer Incoherent Scatter 2000 (MSIS-00) atmosphere model (Picone et al., 2002), in the neutral mass density observations reported at higher altitudes in Liu et al. (2009, 2017), and the 13 MLT peak in NO densities between 120-230 km observed by AE-C (Rusch et al., 1991). From 9 to 16 MLT, there are significantly enhanced NO emissions near the dayside geomagnetic equator, consistent with the general low-latitude NO density enhancement reported from the SNOE mission (Barth et al., 1999). Nitric oxide flux is at a minimum below the auroral ovals at local night where temperatures are low. Additionally, thermospheric neutral wind velocities are lower at night and therefore ion-neutral drag is weaker, so NO has a smaller probability of collision and thus a smaller probability of excitation (Cravens & Killeen, 1988).

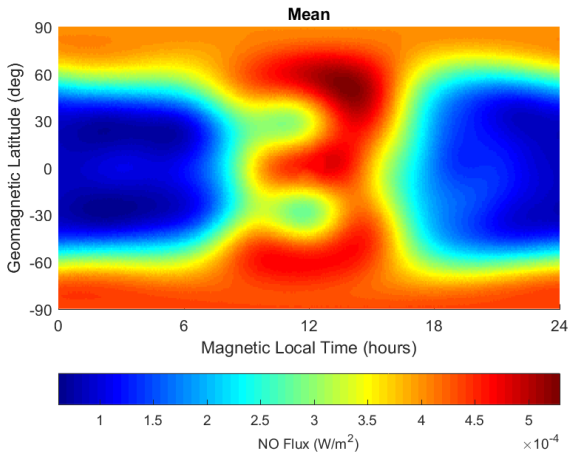

Figure 2: Global mean Nitric Oxide Flux (W/m^2) in geomagnetic coordinates obtained from the SABER 2002-2015 dataset.

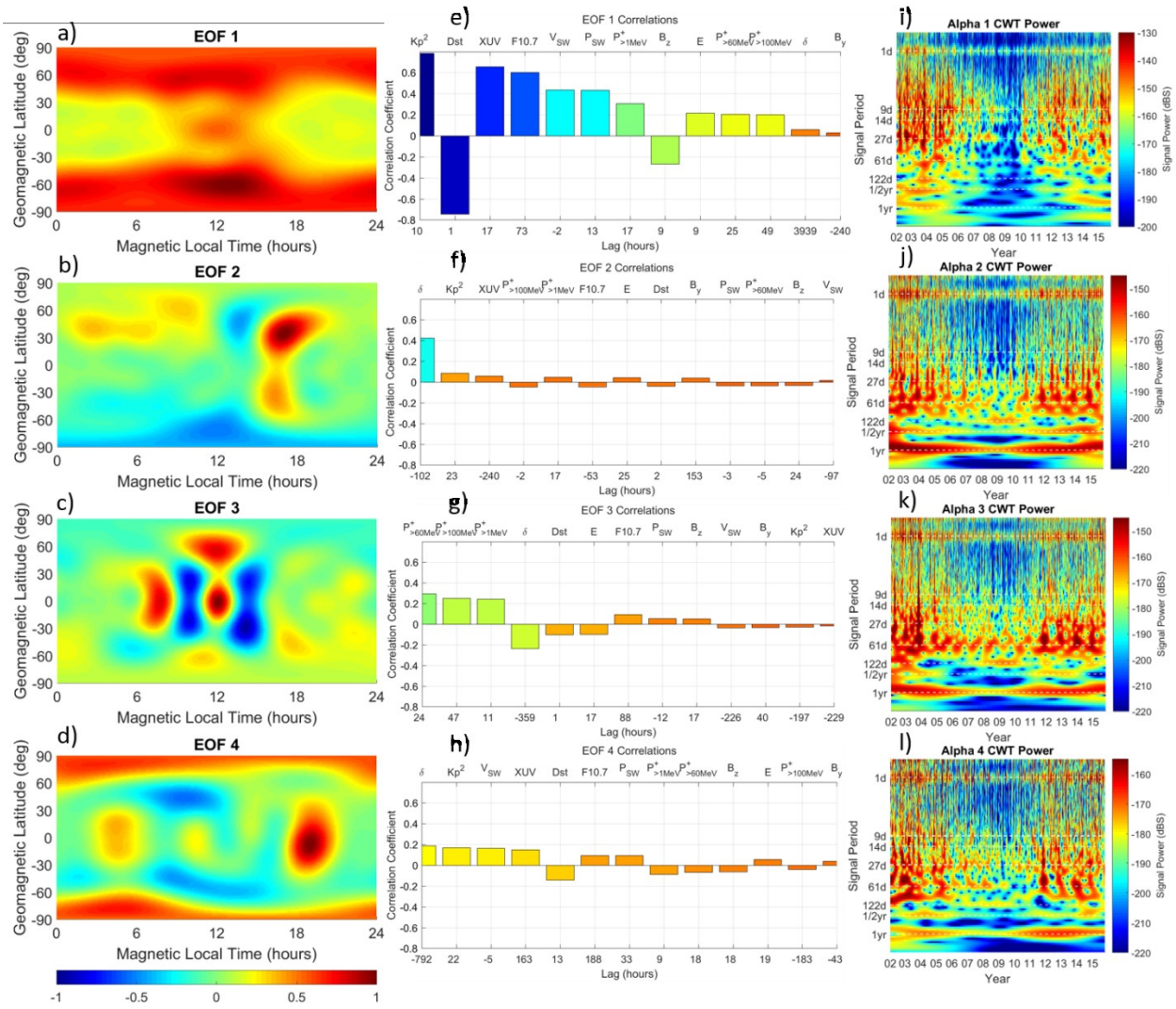

Figure 3: First four nitric oxide flux EOFs (3a through 3d), their correlators (3e through 3h), and their wavelet transforms (3i through 3l). The EOFs are unitless and normalized such that 0 (green) corresponds to no variability in that region. The correlators are ranked by absolute magnitude. Kp^2 is the 24-hour squared planetary K-index; Dst is the disturbance storm time index; XUV and F10.7 are the solar extreme ultraviolet and radio fluxes, respectively; V_{SW} and P_{SW} are the velocity and pressure of the solar wind, respectively; $P^{+}_{>XMeV}$ is the proton flux with energies greater than *X* MeV; B and E are the interplanetary magnetic field and electric field, respectively; and δ is the solar declination angle. The wavelet transforms show signals for periods ranging from 1 day to 1 year. For EOF maps as seen from the geomagnetic poles, see Appendix B.

EOF 1

EOF 1 (Figure 3a) is a completely positive EOF (see color bar) that strongly resembles the mean pattern. The EOF temporal amplitude varies between positive and negative, and tends towards positive around solar maximum (2001 and 2014) and negative around solar minimum

(2008). This EOF shows high variability poleward of ±45° MLAT, particularly within the dayside auroral ovals. The NOF variability is also enhanced at the mid-day equator (10 to 15 MLT).

The strongest variability in this EOF is in the dayside auroral/sub-auroral region. Barth et al. (2001) showed that this geomagnetic latitude band experienced increases in nitric oxide during periods of high geomagnetic activity due to electron precipitation. They also show a longitudinal dependence caused by the longitudinal variation in the magnetic field strength of the auroral oval. They reported that the density of nitric oxide around the auroral zone was non-uniform with the densities at western geomagnetic longitudes enhanced relative to those at eastern longitudes. The local-time presentation likely reveals that these variations are cycling through the dayside where they appear as enhanced variability in the solar-heated thermosphere, possibly explaining the dark red regions of EOF 1.

Correlation analysis of this mode's amplitude (Figure 3b) shows very strong relationships with solar and geomagnetic drivers. Squaring and applying a 24-hour smooth to the Kp index gives a significant correlation coefficient of 0.79 with a 10-hour lag. The Dst and AE indices and interplanetary magnetic field strength (IMF) show similar relationships. XUV radiation has a correlation of 0.66 with a 17-hour lag, and similarly the solar radio flux F10.7 has a correlation of 0.61 with a 2-3-day lag. This EOF shows weaker correlations with solar wind parameters (temperature, velocity, and pressure) of about 0.45, indicating that there is a combination of behaviors in the solar wind (typical of storm time) that creates NOF variability.

Decomposing this EOF's amplitude into wavelets (Figure 3c) reveals strong and noisy signals near the 2001 and 2014 solar maximums (note the full data set and all EOFs also showed

increased noise around solar maximums, and particularly around large solar storms, such as CMEs, high speed streams (HSSs), and solar energetic particle events (SEPs)). There is also a clear 24-hour signal, which is probably a result of the TIMED satellite's daily sampling pattern (it samples all longitudes within roughly the same local time). There appears to be a rough 61-day signal as well, which is probably a combined result of 1) the 61-day MLT and hemispheric sampling period of the satellite, and 2) the regular diurnal variation of NO and other atmospheric constituents (Rusch et al., 1991). There may be effects from migrating and nonmigrating tides as well, which have been observed in the SABER NOF dataset in previous studies (Oberheide & Forbes, 2008; Oberheide et al., 2009; Pancheva & Mukhtarov, 2010; Mukhtarov & Pancheva 2011; Chang, et al. 2016). These sampling artifact signatures appear in all EOF wavelets and will not be discussed further.

There are also periodic signatures of 27-day, 14-day, and 9-day signals in EOF 1. The 27-day signal during solar maximum is likely associated with the 27-day solar rotation of active regions impacting the Earth (Barth et al., 2004). Reorthogonalization and superposed epoch analysis (SEA) of this EOF shows that it peaks after high speed streams impact Earth, which would produce a 27-day signal if they persisted for many months. Additionally, from 2005-2009, three equally spaced and persistent coronal holes corotated about the Sun, creating a disturbance in the thermosphere-ionosphere with a 9-day period (Solomon et al., 2012). Mlynczak et al. (2008) discovered these 6.75-day, 9-day, and 13.5-day periodicities in the SABER NOF dataset from these corotating coronal holes from 2002 to 2006. These coronal holes are associated with high-speed solar wind that deposit energetic particles into the lower thermosphere, influencing NO emissions via changes in temperature, thermospheric composition, and increased collisional energy transfer with atomic oxygen (Mlynczak et al., 2008).

Superposed epoch analysis and storm-specific case studies reveal that EOF 1 peaks positively for Kp ≥ 4 (with up to 12-hour lag), for high-speed CMEs (> 500 km/s) with associated shocks (with about a 12-24-hour lag), after high-speed streams (12-hour lag), after rapid magnetic variations (12-36 hour lag), and after SEP events impact Earth (12-hour lag). This implies that all of these solar-induced events tend to increase NOF with about a 12-hour lag on average. CMEs, solar flares, and high-speed streams have shown to be tied to enhanced NO emissions in previous studies (Knipp et al., 2017; McGranaghan et al., 2014; Mlynczak et al., 2003; Solomon et al., 2012). This is because 1) increased particle precipitation into the auroral zone during moderate and strong storms produces atomic nitrogen (via Equation 1), and 2) thermospheric temperature increases during storm time, which leads to an increased probability of NO collisions with atomic oxygen and subsequent emissions (via Equation 3a) (Liu et al., 2007; Mlynczak et al., 2003).

EOF 2

EOF 2, which represents 7.1% of the total variability in the dataset, exhibits two prominent features: 1) a clear asymmetry between the North and South Hemispheres; and 2) two opposing cells of variability near dusk at ±30° MLAT. In this EOF, the Northern Hemisphere is generally positive and the Southern Hemisphere is generally negative, implying an inverse relationship between the two. The Southern Hemisphere experiences larger variations in NOF (average EOF magnitude of about 0.5 as opposed to 0.1 in the north). EOF 2 also shows a very large mid-latitude shift in NOF just before dusk, around 30° to 60° MLAT. There is a weaker structure in the Southern Hemisphere at this local time as well. The largest flux variability occurs at about 45° MLAT at 16 MLT, just at the edge of strong dayside-to-evening temperature

gradient, and also where Strobel (1971) showed the strongest gradient in ground state nitrogen atoms.

Interestingly, only one of the 30 geophysical indices studied correlates strongly (> 0.1) with this EOF: solar declination (δ), with a correlation coefficient of +0.42, peaking about 4 days ahead of the Summer Solstice. The wavelet decomposition also shows a prominent semi-annual and annual signal throughout the time series. These signals peak positively around the Summer Solstice, and negatively around the Winter Solstice. When combined, the EOF and its amplitude show that there is generally an increase in flux in the summer hemisphere and a decrease in flux in the winter hemisphere.

This EOF may be mainly attributable to annual solar flux variability and its impact on the chemical composition and solar terminator wave variability of the thermosphere. The north-south asymmetry is attributable to the annual hemispherical shift in solar flux due to the Earth's 11° geomagnetic axis tilt combined with the fact that the Earth receives the most solar flux at perihelion, at the Winter Solstice (Qian et al., 2009; Ridley et al., 1999). This EOF shows the most hemispherical variation in the south, perhaps because the geomagnetic South Pole sees more annual variability in solar flux than the geomagnetic North Pole (Marsh et al., 2004).

This EOF peaks positively at the Summer Solstice, and NOF is stronger in the summer hemisphere than it is in the winter hemisphere. However, NO *density* is higher in the winter hemisphere since it is less prone to destruction via solar XUV radiation (Bailey et al., 2004). The EOFs obtained by Marsh et al. (2004) on their altitude-dependent NO densities also revealed a second mode of variability strongly tied to annual variations, with NO density peaks in the winter. However, since N_2 is easily dissociated by photoelectrons, which directly leads to the

production of NO, the NO emissions peak in the hemisphere with the most direct solar flux (i.e., the summer hemisphere).

Next, the opposing structures around mid-latitude dusk are considered, which could be attributable to a terminator wave. The dusk terminator wave produces large meridional (north-south) wind, density, and temperature gradients at the solar terminator between ±30° MLAT in the thermosphere (Liu, 2009). Modeling by Miyoshi et al. (2009) suggested that upward propagating migrating tides generated in the ozone layer by the moving solar terminator are a source of these thermosphere waves. The strength and orientation of these gradients vary annually and seasonally as the solar terminator moves, and are damped by diffusion, conductivity, and ion drag. The effect is most clear during geomagnetic quiet conditions.

Reorthogonalization of these EOFs was performed for various geophysical phenomena, effectively splitting the data set into a much smaller section. When reorthogonalized, EOF 2 shows a much smaller contribution to the covariance than it does for the original dataset, suggesting that this mode of variability only appears for near-continuous sections of data spanning several years. These findings suggest that EOF 2 represents the annual "breathing mode" of NOF, driven by the changes in thermospheric composition, wave variability, and temperature throughout the year.

EOF 3

EOF 3 shows 4 mid-latitude contrasting regions every 2 hours, between dawn and dusk, stretching between ±50° MLAT. It also has a strong structure about 10-20° MLAT below the northern auroral cusp region, which appears to extend to the geomagnetic equator. The Southern Hemisphere has a weaker structure. Like EOF 2, EOF 3 has a weak hemispherical asymmetry.

Since some of these EOF3 structures are in regions that suffer from a lack of data, and are extrapolated based on the surrounding data and spherical harmonics chosen for the EOFs (see Figure 1 and the methods described above), this latitudinal extension near 12 MLT is somewhat suspect.

Correlation analysis of this EOF shows strong (R = 0.24 to 0.30) relationships with energetic proton flux (1-100 MeV) with a ½-day to 2-day lag, and a negative correlation with solar declination (R = -0.24, 15 days ahead of the Winter Solstice). Figure 4 reveals the correlation coefficients and lag times for four levels of energetic proton fluxes for EOF 3, as well as its comparison with the original data and EOF 1 (which also shows a strong correlation with proton flux). EOF 3 did not correlate strongly (> 0.1) with any other geophysical parameter tested. Wavelet frequency decomposition reveals that it exhibits annual variability, with positive peaks around the Winter Solstice and negative peaks around the Summer Solstice, in contrast to EOF 2. Interestingly, reorthogonalization for the 2 months surrounding Winter Solstice shows that the reorthogonalized EOF 2 is composed of 68% of the original EOF 3 and only 14% of the original EOF 2 (Figure 5c), while reorthogonalization around Summer Solstice shows the reorthogonalized EOF 2 is composed of 66% the original EOF 2 and 15% the original EOF3. This implies that EOF 3 is a winter mode that contributes to more NOF variability than EOF 2 does during the winter months.

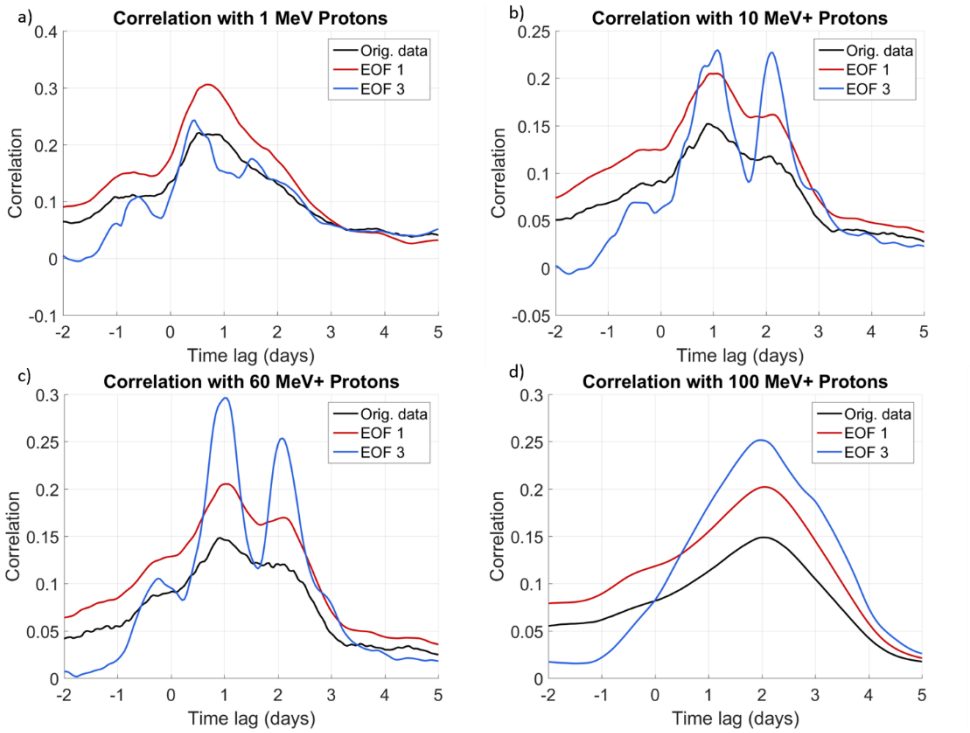

Figure 4: Original NOF data, EOF 1 amplitude, and EOF 3 amplitude correlations and lags with a) 1 MeV, b) 10+ MeV, c) 60+ MeV, and d) 100+MeV proton flux.

Protons with energies near 1 MeV penetrate to the base of the thermosphere at ~ 90 km. Their fluxes are enhanced at Earth by solar flares, CMEs, corotating interaction regions, and shock arrival. These protons have a strong association with energetic storm particles events (ESPs), which are known precursors (~6 hr) of shock arrival (Valtonen et al, 2005). Energetic protons in the 10-100 MeV energy range are mostly produced by fast CMEs moving through the solar corona and out into the interplanetary medium. Occasionally a short burst of energetic particles reaches Earth directly from a solar flare. It is interesting to note that the correlations between the EOF 3 amplitude and solar protons depends on the proton energy. Ten and 60 MeV protons create two peaks in the correlation plot, suggesting that EOF 3 peaks both shortly after a driving activity, such as a SEP event driven by a CME or solar flare, and perhaps peaks again with CME shock arrival (Valtonen et al., 2005). One hundred MeV protons, while typically confined to the polar cap, may have access to auroral latitudes during very strong geomagnetic

storms and cause only one peak in the correlation plot. Appendix C: Movie S1 shows the combined effects of the NOF mean + EOF 1 + EOF 3 surrounding the double CME/SEP event of late October 2003.

Since EOF 1 is strongly tied to CMEs, some of which have SEP events, we should expect some cross-correlation and a physically significant lag between EOF 1 and EOF 3. Indeed, cross-correlation analysis shows that EOF 3 peaks, on average, 5 hours before EOF 1 with a small but clear correlation peak to 0.05. This 5-hour lag is consistent with Valtonen et al. (2005) who report a 6-hour difference between ESP particles and shock arrival. This supports the idea that EOF 3 is related to solar energetic particles and ESPs, since we expect to see maximum SEP impact several hours to a couple days before the onset of a CME and ESPs a few hours ahead of shock arrival. SEPs take less than an hour to several hours to reach Earth, and the SEP event lasts for half a day or more (Zheng & Evans, 2014), while CMEs typically arrive two to three days after an eruption on the Sun.

Reorthogonalization was performed around X-flares, SEP events, Winter Solstice, and SEP events occurring in the winter time (Figure 5). The reorthogonalized EOF 1, which is primarily made up of EOF 1 and EOF 3, shows that emissions are most variable at the daytime auroral oval and at equatorial dawn, dusk, and possibly noon during these types of events. EOF 3 is clearly a strong player for these four types of events. It is most significant during winter-time SEPs: the primary mode of variability surrounding these events is composed of 35% of the original EOF 3.

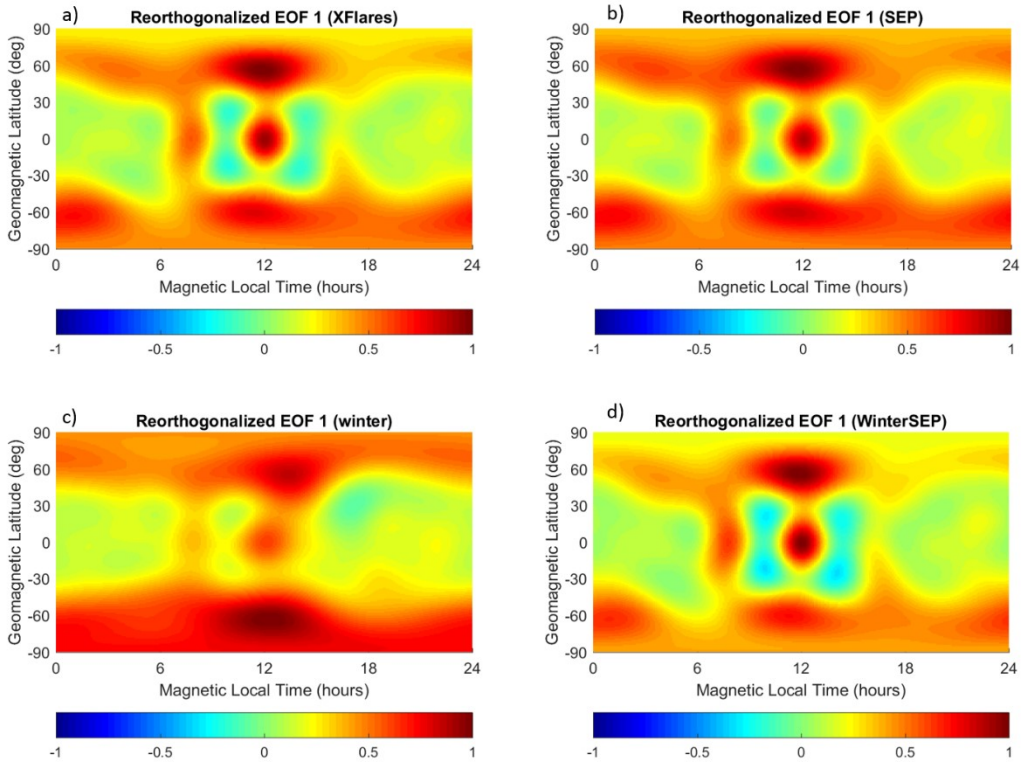

Figure 5: Reorthogonalized EOF 1 for three days surrounding a) X-flares, b) SEP events, c) Winter Solstice ± 30 days, and d) winter SEPs (during Winter Solstice ± 91 days). The new primary mode of variability for X-flares represents 64% of the total variability, and it consists of 59% the original EOF 1 and 28% the original EOF 3. The new primary mode of variability for SEPs represents 62% of the total variability, and it consists of 65% the original EOF 1 and 22% the original EOF 3. The new primary mode of variability for Winter Solstice represents 67% of the total variability, and it consists of 71% the original EOF 1 and 8% the original EOF 3. The new primary mode of variability for winter time SEPs represents 70% of the total variability, and it consists of 52% the original EOF 1 and 35% the original EOF 3.

SEPs have only been documented to produce NO in the 40-80 km region; 20 km below SABER's lower bound (Sinnhuber, 2012). These SEPs pass through the thermosphere most directly via the magnetic flux tubes, which intersect the thermosphere at and above the auroral cusp latitude, about 10° poleward of the red funnels seen in the north and south in EOF3. Even though SEP protons are unlikely to directly enhance NOF variability from 100-250 km, it is still likely that the SEPs are producing an indirect effect in the lower thermosphere.

Marsh and Russell (2000) describe variability in the low-latitude (between ±60°) dawn and dusk NO mixing ratios taken by the HALOE experiment in the mesosphere and lower

thermosphere (80 to 130 km) due to seasonal and annual vertical migrating (Sun-synchronous) diurnal tides. These tides show altitude, latitude, and local-time dependencies, which affect NO on both large and small timescales. Additionally, Trifonov et al. (2016) describe a process by which solar proton events *strengthen* these migrating semidiurnal and diurnal tides in the mesosphere and lower thermosphere by changing the wind and temperature regime of that region. The powerful SEPs they studied affected mesosphere/lower thermosphere winds in the winter season, consistent with the winter SEP correlation with EOF 3. Jackman et al. (2007) explain how SEPs change the chemistry of the mesosphere, producing heating and cooling rate changes and a perturbation of zonal (east-west), meridional (north-south), and vertical winds in their models. SEP-induced wind and temperature effects last for 4-6 weeks in the mesosphere (Jackman et al., 2007), the effects of which may propagate into the lower thermosphere via the vertical component of the migrating diurnal tides. Thus, EOF 3 may be driven by these annual and seasonal tides, which are enhanced during and long after the onset of solar proton events, particularly in the winter.

EOF 4

Although EOF 4 only represents 2.3% of the total variability, it reveals some subtle yet interesting patterns that provide a global context for SNOE observations. EOF 4 shows strong variabilities at the poles and two strong equatorial cells of variability, one pre-dawn and one post-dusk. Additionally, the daytime subauroral regions show an opposing variability. Interestingly, correlation analysis shows a relationship with solar declination (R = +0.19, 33 days ahead of Summer Solstice), and several very weak (0.1 to 0.2) geomagnetic (AE, Kp, AL, Dst,

B) relationships with this EOF (note that the solar correlators; solar wind speed, XUV, and F10.7; have inconclusive peaks in their correlation plots).

The strongest geophysical correlations for these parameters are comparable to those in EOF 1, but with an additional lag of around 12 to 20 hours. This suggests an atmospheric transportation mechanism following the primary stages of a geomagnetic storm: initially, EOF 1 peaks, increasing flux globally, but particularly at the auroral ovals between dawn and dusk (note that superposed epoch analysis where $Kp \geq 6$ shows that EOF 4 peaks negatively when EOF 1 peaks positively, initially enhancing auroral NOF). About 12 hours later, EOF 4 peaks positively, indicating that NOF is moving away from the auroral and subauroral regions. Appendix C: Movies S2-S5 show the combined time-series behavior of the NOF mean + EOF 1 + EOF 4 for four storm events.

Barth and Baily (2004) describe SNOE observations that imply NO transport in the pre-noon sector that is consistent with this EOF4 variability. On high-geomagnetic-activity days (Kp =8), NO was transported from the auroral zone all the way to the equator. The NO transport is seasonal, with the most effective transport in the fall-winter hemisphere. These maps provide a more global context for the variability (and likely transport) of NO.

Knipp et al. (2017) also show a latitudinal expansion of NOF in the 1-3 days following CMEs. The thermospheric model produced by Demars and Schunk (2007) also shows that Joule heating causes vertical transport of neutral density and diverts it both poleward and equatorward. Furthermore, Richards (2004) explains how NO density increases at auroral latitudes first, and then at mid-latitude night due to aurorally-enhanced equatorward winds after a geomagnetic

storm, triggering a negative ionospheric storm. EOF 4 is a very strong player (> 10% of explained variability) in EOF reorthogonalization surrounding large sign changes in B_y.

The wavelet decomposition of EOF 4 shows two interesting features: 1) a 27-day period at solar minimum, and 2) a strong annual signal at solar maximum. The former signal may be attributable to high speed streams, which would cause a 27-day effect at solar minimum. The latter may be due to sign changes in IMF B_y, which are seasonal and strongest at solar maximum. The thermospheric density enhancements and energy deposition caused by high speed streams are also seasonal, with the largest enhancements being found in thermospheric neutral densities and SABER NOF data at the equinoxes (McGranaghan et al., 2014; Mlynczak et al., 2008). However, other than the strong component of EOF 4 in large reversals of B_y, there is no strong component of EOF 4 at the equinoxes or during high speed streams.

Chapter VI

Further Discussion

The first four EOFs have been interpreted in terms of possible geophysical drivers using correlation analysis, superposed epoch analysis, reorthogonalization, and previous research. The mean NOF map shows enhanced emissions at the auroral ovals and on the dayside between dawn and dusk, probably resulting from regular auroral electron precipitation and the temperature-dependent chemistry of NO production and emissions. EOF 1 is correlated with nitric oxide production and excitation via geomagnetic and solar drivers, including geomagnetic storms and soft solar X-ray flux. EOF 2 oscillates annually and seasonally, indicating a large-amplitude, low-frequency "breathing mode" based on annual thermospheric chemistry, such as density and temperature variability. EOF 3 may be driven by migrating diurnal tides that become enhanced following SEP events, particularly in the winter months. EOF 4 represents a transport mechanism towards the poles and extending into pre-dawn and post-dusk following the EOF 1 variability after strong geomagnetic storms. However, there are other mechanisms which may play a role in generating the patterns displayed here.

Mean Map: Further Discussion

The mean map shows the global extent of NO 5.3 μm flux, which is a convolution of NO density, thermospheric composition and temperature, and neutral transport. Many features of the mean pattern are consistent with previous zonal-averaged profiles from SNOE NO density observations (i.e., Marsh et al., 2004). These were limited to the pre-noon sector. The strong emissions poleward of the auroral regions are probably driven by precipitating auroral electrons that ionize and dissociate N_2 into atomic nitrogen that can react with oxygen to produce NO.

Given the mid-morning gaps between auroral and equatorial emissions, the elongated structure at the daytime equator is likely not caused by equatorward transport but rather by solar XUV interactions. XUV creates photoelectrons in the low-zenith-angle upper atmosphere that dissociates molecular nitrogen into atomic nitrogen, a key ingredient of NO production. These energetic electrons also heat the atmosphere, thus aiding in production of NO and its emission (Barth et al., 1999).

The mean map shows hemispherical asymmetry centered at ±50° MLAT at 14 MLT. On average, the northern region shows about 113% the flux of the southern region. This difference is not made up in subsequent modes of variability: in fact, the original SABER data set gives the same ratio to within 1%. There are at least two possible reasons for this hemispherical asymmetry:

1. Biases in the dataset: when TIMED was in one of these regions, it had a 5% greater chance of being in the summer months. This would produce a slightly biased plot from the tilt of the Earth at this time, which may increase NO emissions in the Northern Hemisphere and decrease them in the Southern Hemisphere.
2. Hemispheric asymmetries in the geomagnetic field: as noted in Luan et al. (2016), the average daily peak hemispheric power is 19% larger in the Northern Hemisphere than in the Southern Hemisphere. Additionally, there is supporting evidence of dayside energy asymmetries from the CHAMP density anomalies at the auroral cusps (75-80° MLAT, about 25-30° higher than the structures shown here), which showed 1.35 times stronger signatures in the north, independent of solar wind and solar flux differences (Rentz & Lühr, 2008). This may be due to the larger physical offset between the geographic and geomagnetic south poles causing the southern cusp density to disperse more (Rentz &

Lühr, 2008). These hemispherical density effects may affect the lower latitudes where the hemispherical differences are observed in the mean map.

EOF 1: Further Discussion

The spatial variations displayed in EOF 1 are expected during geomagnetic and solar storms, when NO production increases globally and particularly in the auroral regions with a 1-day lag and a 2-3-day emission duration (Barth, 2010; Barth et al., 2009; Lu et al., 2010; Marsh et al., 2004; Mlynczak et al., 2003; Oberheide et al., 2013; Weimer et al., 2015). These storms increase Joule heating and global neutral densities in the lower thermosphere, which aid in 1) producing NO through the high-temperature reaction between N and O_2 above 140 km (Equations 1, 2a, and 2b), and 2) increase the kinetic energy of constituents, allowing molecules like NO and O to collide, causing NO to excite and emit (Equations 3a and 3b) (Mlynczak et al., 2003; Rentz & Lühr, 2008; Richards, 2004). Atomic oxygen densities also increase during solar maximum, increasing the likelihood of collision with NO, resulting in a spontaneous emission (Jones et al. 2016; Mlynczak et al., 2003). Additionally, particle densities and energies have been shown to increase at high latitudes and in the polar regions with increasing geomagnetic activity (Jacchia & Slowey, 1963; Liu et al., 2005). In the altitude-dependent EOF analysis of SNOE NO densities, Marsh et al. (2004) also found the first mode of variability to be associated with auroral NO production above 30° MLAT, which represented 45.2% of their total variability. His team found strong correlations with geomagnetic activity (Kp index, $R = 0.776$) and solar flux ($\log_{10}$(F10.7), $R = 0.654$) with about a 1-day lag. Lu et al. (2010) found that the peaks in NOF lagged behind Kp and F10.7 peaks by about one day as well. This EOF correlates with XUV with a 1-day lag, and with F10.7 with up to a 3-day lag in NO emissions. Once NO is created, it

may take another full rotation into the sunlight before it starts emitting, resulting in the 2-3-day lag with F10.7 (Richards, 2004).

EOF 1 shows enhanced variability at the daytime equator. This may be caused by solar soft X-rays impacting lower latitudes and helping to create NO via secondary electrons, which increases NOF with about a 1-day lag (Barth et al., 2003, 2009; Jones et al., 2016; Marsh et al., 2004; Weimer et al., 2015). Alternatively, the TIE-GCM model results from a study by Jones et al. (2016) revealed a significant tidal impact on 100-200 km NOF at solar maximum, with the most solar-cycle variability centered over the equator. This variability is independent of solar soft X-ray flux (Jones et al., 2016) and may contribute to the enhanced variability at the equator in EOF 1.

Ridley et al. (1999) found that the NO mixing ratio increases equatorward as magnetic activity increases. The addition of EOF 1 to the mean NOF map reveals that NOF expands from about ±60° MLAT (shown in the mean map) down to ±40° MLAT with increasing geomagnetic and solar activity. It is then possibly transported to ±30° MLAT via meridional winds at the time of the solar flux peak, around 14 MLT (Barth et al., 2004).

EOF 2: Further Discussion

EOF 2 may represent the "breathing mode" of NOF variability due to annual and seasonal thermospheric composition and temperature changes. Qian et al. (2009) describe many different geophysical processes that affect the annual and seasonal variability of global thermospheric temperature, density, composition, and scale height variations (Hedin et al., 1977; Paetzold and Zschörner, 1961), including: geomagnetic activity peaks at the equinoxes (Walterscheid, 1982),

large-scale semiannual interhemispheric circulation (Fuller-Rowell, 1998), annual variability of total electron content (TEC) (Mendillo et al., 2002), and eddy mixing (diffusion and turbulence) in the mesopause due to seasonal variations in gravity wave breaking (Qian et al., 2009). Jones et al. (2014, 2016) also describe annual and seasonal variability of multiple thermospheric constituents, including NO, O, O_2, and N_2 due to vertical tide-induced thermospheric temperature variations. These tides affect temperature the most at the equinoxes and depend strongly on the solar cycle (Jones et al., 2016). In summary, all of these processes may directly or indirectly affect NO emission rates through EOF 2: an increase in NO density, O density, $N(^2D)$ density, O_2 density, and thermospheric temperatures directly drive NOF production (Bailey et al., 2004; Jones et al., 2016; Mlynczak et al., 2003), which are all partly driven by the annual and seasonal variations in Earth-Sun distance and solar zenith angle, geomagnetic activity, interhemispheric circulation, TEC, eddy diffusion, and gravity-wave breaking.

The thermospheric diurnal tides have similar structural characteristics to EOF 2 and its signatures have been previously found in SABER data. Chang et al. (2016) provide amplitudes and variabilities of the nonmigrating (non-Sun-synchronous) diurnal DE3 tide in COSMIC TECs, which vary around ±30° MLAT, cycle seasonally at the equinoxes, and depend on solar activity. Signatures of DE3 were observed in TIMED SABER thermospheric temperatures (Oberheide & Forbes, 2008; Oberheide et al., 2009; Pancheva & Mukhtarov, 2010). Mukhtarov and Pancheva (2011) also found prominent DE3 tides peaking June-October and March. DE3 is the strongest diurnal tide from 110-115 km, near the region of highest NO densities and emissions (Mukhtarov & Pancheva, 2011). It may be related to the DE3 tides in electron density, which are driven by the diurnal changes in photo ionization and vary annually (Mukhtarov & Pancheva, 2011). Oberheide and Forbes (2008) also reveal strong influences of wave-3 and

wave-4 nonmigrating tides (DE2, SE1, and DE3) on SABER NO variability and neutral gas density between 30°S to 30°N at 100-135 km altitude. Additionally, Chang et al. (2016) describe the migrating (sun-synchronous) tides (diurnal DW1) peaking between ±30° MLAT twice per year centered in the summer hemisphere. Mukhtarov and Pancheva (2011) describe DW1 and SW2 tidal signatures in SABER temperatures. Since these EOFs are calculated in solar coordinates (MLT), we expect to see the effects of migrating tides (DW1 and SW2, which are Sun-synchronous). The effects from nonmigrating (non-Sun-synchronous) tides are expected to be dispersed and spread-out in MLT in this domain. Although EOF 2 shows MLT-dependent structures between ±30° MLAT that cycle annually and seasonally, it is difficult to tie these to a specific tide, because 1) thermospheric tidal waves interfere with one another; and 2) the EOF 2 amplitude is contaminated by other signals and biases; i.e., it is dependent on the geographic and geomagnetic longitude and latitude of the spacecraft, with spikes occurring at the 61-day yaw maneuvers.

Neutral wind fields at 120 km produced using the NCAR TGCM model produce two circular cells near the polar caps that vary annually and expand during geomagnetic active times, possibly pushing NO equatorward (Cravens & Killen, 1987). An alternative to the annual chemistry or seasonal tides discussed for EOF 2 may be related to various wind patterns and convection cells like these.

EOF 3: Further Discussion

NO production is highly dependent on atomic nitrogen density, which is produced via dissociation by energetic electrons (Richards, 2004). Some SEPs are electron-rich. As the protons and electrons from a SEP pass through the thermosphere, they may ionize the

thermospheric constituents and create free energetic electrons at high latitudes. These electrons have the capability of 1) dissociating N_2, which then aids in the production of NO, or 2) they may directly collide with NO, causing it to emit. The maximum ionization rate in the funnel-like structure of EOF 3 (between 100-250 km at 55-60°N) is about 5e7 $m^{-3}s^{-3}$ for protons and about 5e8 $m^{-3}s^{-3}$ for electrons during geomagnetically quiet conditions (Wissing & Kallenrode, 2009). However, Wissing and Kallenrode (2009) show that during the SEP events of October/November 2003, proton ionization and electron ionization in this region increase by factors of up to 20 and 10, respectively. In this case, electron ionization rates far exceeded those of protons for the 100-250 km region: electron ionization contributed to more than 90% of total ionization by either electrons or protons. Therefore, while SEPs cause ionization and significant NO emissions in the mesosphere (Sinnhuber, 2012), electron-rich SEPs may also contribute to dissociation of nitrogen and NO emissions in the thermosphere.

EOF 4: Further Discussion

EOF 4 shows movement away from the auroral regions following strong geomagnetic storms. NO densities have shown to transport from the auroral regions to the equator for strong storms (Barth & Bailey, 2004). Equatorward transport of NO is probably inhibited by dayside poleward winds. Thus, only during strong storms would dayside transport to the equator be successful (Flynn, 2017). However, in the dawn and dusk regions (which were not sampled by SNOE) such transport may be more efficient and successful at lower levels of geomagnetic activity, possibly driven by more solar wind forcing from high speed streams (Flynn, 2017). Further, in these nighttime regions photodissociation of the transported NO is unlikely; thus, transported NO would have a longer lifetime. This may explain the cells of variability at the equatorial pre-dawn and post-dusk regions.

Chapter VII

Model Validation and Error Analysis

K-Fold Cross Validation

The simplest way to validate these EOFs is by plotting their eigenvalues along with errors bars and check that no two eigenvalues overlap, as explained in North (1982). However, the large number of data points shrinks these error bars to very small values, and the analysis becomes useless. Instead, k-fold cross-validation is applied to the EOFs to help determine the confidence and uncertainty associated with each EOF.

K-fold cross-validation splits the data up into k training and testing sets, providing a bias-variance trade-off, as described in James (2015). K-fold cross-validation works by randomly splitting up the data of size L into k complementary equal-size chunks, or folds. Each L/k-sized subset of the data is a validation set to the complementary $(k-1)Lk^{-1}$ sized training set. The EOF regression technique is applied to each training set, and the results are used to predict the behavior of each corresponding validation set. The mean or median of the validation results in terms of RMSE are then taken (Flynn, 2016; James, 2015). Traditionally, this validation technique is applied randomly to non-time series data. However, for time series data, the training sets can be split up using forward chaining, or can be determined systematically from the data to ensure a smooth time series for each set. For this study, the latter method was used. The data set was split up into five validation sets by sampling every 5th data point. The five training sets are the complements of these. The percent error between the full data model root-mean square error (FRMSE) and the median of the five validation set RMSEs (VRMSE) is defined as:

$$\%\ Error = median(|FRMSE - VRMSE_k|) \times 100 / FRMSE \qquad (7)$$

Figure 6 shows how the confidence decreases and uncertainty rises as EOFs are added to the model for a smaller set of data. As EOFs are added to the training set model, the RMS errors in the omitted validation set decrease, as expected. However, as EOFs are added, the deviations between the full data set model (in terms of FRMSE) and the k-folds (in terms of median VRMSE) starts to increase, indicating that these EOFs may not be valid additions to the EOF model. In summary, although adding EOFs to the model reduces RMS error, the model starts to deviate away from what the full data set shows. The first four EOFs produce a median VRMSE within 99% of the FMRSE, while five EOFs produces a VRMSE that is still within 98% of the FMRSE.

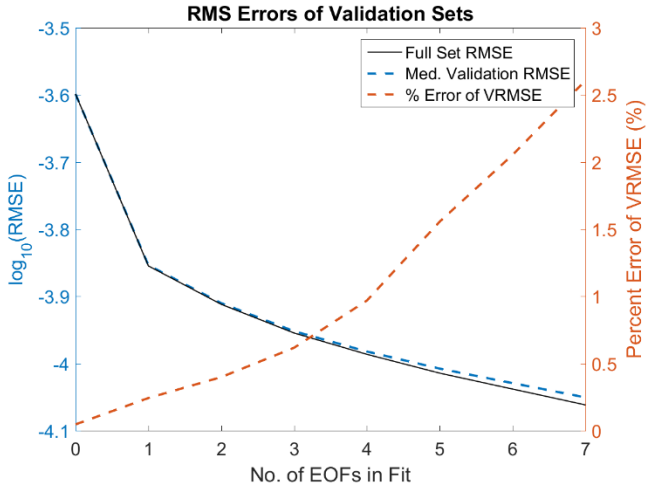

Figure 6: Log_{10} plot of full data set RMSE in solid black and median validation set RMSE in dashed blue, and percent error between them in red.

The e-folding temporal scales of the autocorrelation of EOF amplitudes may also help to understand the persistence of an EOF and its coherency over time. The large-scale modes (i.e. EOF 1) have the longest persistence, as has been demonstrated for high-latitude electrodynamics by Matsuo et al. (2005). The e-folding timescales of EOFs 1 through 7 are displayed in Table 2.

The first three EOFs have e-folding time scales longer than a day, while higher-order EOFs have time scales shorter than a day.

EOF	1	2	3	4	5	6	7
Autotemporal Scale	75d	5.4d	1.4d	7.1h	5.0h	4.8h	3.9h

Table 2: e-folding timescales of EOFs 1 through 7.

Model Performance, Limitations, & Sources of Error

A time series of this data reconstructed along the satellite path shows qualitatively where the model performs poorly (See Appendix C: Movies S6, S7, and S8). Specific case studies of model performance are analyzed as well (Appendix C: Figure A2), in which four periods of differing solar flux, geomagnetic activity, and storm status are analyzed, since these directly and indirectly drive NO production, destruction, and emissions. Poor performance normally occurs in places where there is low NOF, like near the equator, at night, and during solar minimum. Sometimes the NOF reconstructed along the satellite path goes negative, but when a 1-orbit smoothing filter is applied, the error decreases and the model performs quite well physically.

There are several different data and model limitations that are worth discussing. There exists 1) sparsity, bias, and sampling issues in the original dataset, 2) noise and instrument error, and 3) assumptions made about EOF analysis.

1) Sparsity, bias, and sampling issues:

As shown in Figure 1, SABER's spatial distribution of NO emissions is not evenly distributed over the globe. It is biased towards local night between ±53° due to the satellite's orbit and instrument slews. There is very little data at local noon due to spacecraft yaw maneuvers and along the equator due to CGM unit conversions. Additionally, the spacecraft

covers all geographic longitudes in a 24-hour period, but it takes 61 days to cover all magnetic local times, at which time the spacecraft slews to point SABER at the other hemisphere. This may introduce sampling issues and bias in the EOFs, as some regions are weighted more than others. These sampling issues also introduce periodic signals (24-hour, 61-day, and 122-day) into each EOF amplitude, as discussed earlier.

The NOF has been integrated from 100-250 km in 1 km steps. The EOF analysis presented here provides a 2-dimensional spatial view of NOF variability, but does not take into account how NOF varies over this altitude range. It is highly likely that by viewing NOF variability this way, any altitude-dependent variance in the dataset is being overlooked.

Lastly, it is important to point out that each measurement is one snapshot in time and space; thus, one event cannot be completely captured by the SABER instrument. EOF analysis attempts to piece these individual observations together and interpolate into global NOF maps over the full timeframe.

2) Instrument noise and other errors:

The resolution of NOF taken by the SABER instrument can be defined by the noise in the data and unknown systematic errors. Random noise in the dataset, which has an amplitude of about 4e-9 W/m^2, should average out and not affect the EOFs, since the EOFs aim to extract the largest periodic modes of variability. The standard deviation of the first four EOF amplitudes are on the order of 1e-4 W/m^2, well above the random noise floor. During each 61-day yaw maneuver, artificial spikes were observed in the data set, and these appear in all EOF amplitudes.

Although the NOF data was integrated from 100-250 km, the height of peak emissions at 130 km was chosen for the AACGM conversions. This may introduce up to a 3° uncertainty in the geomagnetic coordinates of the SABER NOF and resulting EOFs.

There are unknown errors associated with the NOF volume emission rates as derived from the spectral bandpass of SABER and the extrapolation/derivation method (Mlynczak et al., 2003). However, these methods are not thought to affect NOF spatiotemporal variability (Mlynczak et al., 2003).

3) EOF technique pitfalls:

Although EOF analysis provides an effective data reduction technique, a noise reduction tool, and a means for predictive modeling, it is sensitive to sampling issues and the shape of the domain (discussed above) and results may be geophysically misinterpreted (Björnsson & Venegas, 1997). Correlation analysis, superposed epoch analysis, and EOF reorthogonalization are used to support the geophysical associations, but it is possible that the geophysical modes are dependent and correlated, and therefore "mixed" within the EOFs. This is most notable in EOFs 2 and 3, which have several plausible geophysical drivers.

The NOF data distribution is exponential, with lower flux values being the most common. This puts the mean NOF on the lower end of possible NOF values, so when EOFs based on spherical harmonics are fit to the residuals, they may overshoot in the negative direction, causing the model to become negative. Although this is still statistically sound, physically it makes no sense. If needed, these values can be floored at an appropriate minimum flux of 5e-11 W/m^2, the value of the minimum flux observed in the SABER data set (Flynn et al., 2016).

EOF analysis does not take into account the data distribution. The SABER NOF data set has very few data points around local noon and at the poles, but the EOFs produce continuous interpolated and extrapolated NOF maps over the globe. This is important to remember when utilizing and analyzing the EOF model.

Chapter VIII

Future Work

There are two major elements of future work: 1) improvements of the EOF method, and 2) further exploration of the NOF model domain.

One of the downsides to the EOF analysis performed here is that sometimes the NOF fit becomes negative, which does not physically make sense. One way to avoid this in the future is to put a constraint on each consecutive EOF fit that ensures the model is always positive.

Richards (2004) argues that thermospheric NO chemistry and transport depend on altitude. He argues that equatorward transport of NO may only occur below 150 km. In his model, NO above 150 km is primarily produced via storm effects and Joule heating. Once it rotates into the sunlight, it is destroyed via disassociation before it has time to travel to lower latitudes. However, it can diffuse downwards to 110 km within about a day of the storm, where it lasts for more than a day and may be transported to lower latitudes. In the analysis done here, this horizontal transport (but not vertical) may be shown by the combination of EOF 1 (auroral enhancements at storm time + 12-24 hours) and EOF 4 (enhancements spread both poleward and along the equator into dawn and dusk, ~12-20 hours after EOF 1 peaks). Splitting up the EOFs in the altitude domain may further support Richards's (2004) hypothesis.

Jones et al. (2016) describe meridional (north-south) and vertical tidal transport of NO due to zonal-mean (east-west) winds. Upward propagating tides and gravity waves can cause an upwelling of energy into the thermosphere, disrupt ionosphere-thermosphere circulation, and change the densities of atmospheric constituents as well (Chang et al., 2016; Barth et al., 2009; Jones et al., 2016; Oberheide et al., 2013). Oberheide et al. (2013) and Oberheide and Forbes

(2008) also show longitudinal variability in NO from non-migrating (non-Sun-synchronous) tides. The lifetime of NO due to tidal transport is on the order of 10 days near 100 km, but less than a day above 125 km during solar minimum conditions. The tidal effects are significant: in the TIE-GCM simulation performed by Jones et al. (2016), NO in the 100-200 km altitude region increased up to 120% (40%) at solar minimum (maximum). In the EOF analysis presented here, variability due to vertical or zonal forces, such as these tides, is washed out due to the two-dimensional geomagnetic domain chosen. Analyzing the EOFs for different altitude bands or in geographic coordinates may reveal interesting tidal effects.

Marsh et al. (2004) expanded on their altitude-dependent NO density EOF analysis by creating predictive models. Since their first three EOFs correlated strongly and independently with different geophysical drivers (Kp, solar declination, and F10.7), they were able to obtain significant correlation coefficients and determine predictive models. If the EOFs presented in this paper can be better quantified by independent geophysical phenomena, such as through further reorthogonalization or kernel PCA analysis, they may be used as a predictive model of NOF in the future.

Chapter IX

Conclusions

The first four EOFs capture 83% of the total variance in the TIMED SABER NOF data set. The mean NOF and four EOFs reconstruct a global NOF map, compressing the 13 years of SABER NOF data down to 6% of its original size. Additional analysis of the EOF amplitudes using correlation analysis, wavelet-based frequency analysis, superposed epoch analysis, and reorthogonalization have helped to determine the possible geophysical drivers for each EOF. The mean NOF map (Figure 2) shows that nitric oxide emissions in the thermosphere are regularly driven by solar and auroral drivers. NO emissions are strongest between dawn and dusk, peaking around local noon. NO also emits poleward of the auroral ovals at all times, and peaks at all geomagnetic latitudes at 14 MLT.

- **EOF 1** has strong correlations with indicators of **solar flux and geomagnetic storms**. Its amplitude correlates with the smoothed and squared Kp index (R = 0.78 with a 10-hour lag), and correlates similarly with AE, AL, Dst, and IMF. It also correlates strongly with XUV (R= 0.66 with a 17-hour lag) and other solar fluxes (F10.7, FUV, MUV, TSI). The spatial structure of this EOF shows that during storm times, NOF increases over the whole globe with a 12-24 hour lag, particularly at the auroral ovals and during the day time. This EOF represents 69.2% of the total variance of the original data set, suggesting that NOF variability is mainly driven by solar flux and geomagnetic storms.

- **EOF 2** exhibits **annual and seasonal variations** that may be caused by the seasonal variability in thermospheric densities, wave behavior, and temperature. This EOF, which

accounts for 7.1% of the total variance, may represent the large-scale "breathing mode" of NOF as the thermosphere changes throughout the seasons, affecting NO production and chemistry. A dusk terminator wave representing large changes in chemistry (temperature and densities) may also affect this EOF. EOF 2 correlated strongly (R = +0.42) with solar declination angle, but not with any of the other 30 geophysical or solar indices tested, and represented significantly reduced variability for subsets of data.

- **EOF 3** is associated with **solar proton flux** (R = 0.24-0.30, 1/2-2-day lag) and has an annual variability with peaks in the winter. This EOF peaks following X-flares and SEPs, particularly in the winter time. The structure of this EOF is consistent with migrating diurnal tides, which become enhanced in the lower thermosphere after SEP events, particularly in the winter months. This EOF accounts for 4.2% of the total variance.

- **EOF 4** represents 2.6% of the total variance, and correlates weakly with many of the same geomagnetic drivers of EOF 1 but with a later lag of 12-20 hours. The progression from EOF 1 to EOF 4 may be driven by **thermospheric transport mechanisms**. This EOF may provide insight into the lasting effects on the thermosphere after a storm. EOF 1 shows that the whole thermosphere glows with NOF 12-24 hours after a storm, particularly at the auroral ovals and during the daytime. About 12-20 hours later, EOF 4 shows that the polar caps experience an increase in flux, and the effects extend weakly into the pre-dawn region and significantly into the post-dusk region. The initial increase in flux at the daytime auroral ovals is depleted slightly as the excited NO is transported to the poles and extended in MLT.

EOFs 5 through 7 do not appear to show any meaningful or strong correlations with geophysical drivers. Additionally, after EOF 4, the drop in the percentage variance explained by each additional EOF starts tapering off, suggesting that 1) noise and geophysical cross-contamination may have an effect, and 2) the model may over-fit if these were to be included. The model was validated using 5-k-fold cross-validation. Although adding EOFs to the model decreases the overall RMSE, it increases the percent error in median RMSE of the 5 validation sets. The first 4 EOFs produce a median validation set RMSE within 99% of the full data set's RMSE, which may be a good indicator of the point at which the model is well-fitted.

This work is the first to explore global thermospheric NOF variability in the global geomagnetic latitude and magnetic local time domain. The global NOF EOF analysis performed in this paper, along with the correlation analysis, provides significant insight into the spatiotemporal distribution of NOF variability and how it ties to geophysical drivers. This data compression technique may also be useful in developing computationally-efficient data assimilation of the NOF data set in future studies. Furthermore, the correlation and wavelet analysis performed on the EOF amplitudes can be used to develop a future predictive model of nitric oxide flux, ultimately contributing to a global thermospheric temperature model.

Bibliography

Bailey, S. M., Rodgers, E. M., Yonker, J., Barth, C. A., & Baker, D. N. (2004). The Observed Response of the Lower Thermosphere to Solar Energetic Inputs. *LWS Workshop March 24, 2004.* PowerPoint Presentation.

Barth, C. A. (1992). Nitric oxide in the lower thermosphere. *Planetary and Space Sciences*, 40, 315—336. http://dx.doi.org/10.1016/0032-0633(92)90067-X

Barth, C. A. (1995). Nitric oxide in the lower thermosphere, in The Upper Mesosphere and Lower Thermosphere: A Review of Experiment and Theory. *Geophysical Monograph Series*, vol. 87, AGU, Washington, D. C.

Barth, C. A. (2010). Joule heating and nitric oxide in the thermosphere. *Journal of Geophysical Research*, 115, A10305. http://dx.doi.org/10.1029/2010JA015565

Barth, C. A., & Bailey, S. M. (2004). Comparison of a thermospheric photochemical model with Student Nitric Oxide Explorer (SNOE) observations of nitric oxide. *Journal of Geophysical Research*, 109, A03304. http://dx.doi.org/10.1029/2003JA010227

Barth, C. A., Bailey, S. M, & Solomon, S. C. (1999). Solar-terrestrial coupling: Solar soft x-rays and thermospheric nitric oxide. *Geophysical Research Letters*, 26(9), 1251-1254. http://dx.doi.org/10.1029/1999GL900237

Barth, C. A., Baker, D.N., & Bailey, S. M. (2004). Comparison of a thermospheric photochemical model with Student Nitric Oxide Explorer (SNOE) observations of nitric oxide. *Journal of Geophysical Research*, 109, A03304. http://dx.doi.org/10.1029/2003JA010227

Barth, C. A., Baker, D. N., Mankoff, K. D., & Bailey, S. M. (2001). The northern auroral region as observed in nitric oxide. Geophysical Research Letters, 28(8), 1463-1466. http://dx.doi.org/10.1029/2000GL012649

Barth, C. A., Lu, G., & Roble, R. G. (2009). Joule heating and nitric oxide in the thermosphere. *Journal of Geophysical Research, 114(*A05301). http://dx.doi.org/10.1029/2008JA013765

Barth, C. A., Mankoff, K.D., Bailey, S. M., & Solomon, S.C. (2003). Global observations of nitric oxide in the thermosphere, *Journal of Geophysical Research*, 108(A1), 1027. http://dx.doi.org/10.1029/2002JA009458

Bermejo-Pantaleón, D., Funke, D., López-Puertas, M., García-Comas, M., Stiller, G. P., con Clarmann, T., … Lu, G (2011). Global observations of thermospheric temperature and nitric oxide from MIPAS spectra at 5.3 μm. *Journal of Geophysical Research,* 116, A10313. http://dx.doi.org/10.1029/2011JA016752

Björnsson, H. & Venegas, S.A. (1997). A manual for EOF and SVD analyses of climate data. *CCGCR Report No. 97-1,* Montréal, Québec, pp. 52.

Chang, L. C., Sun, Y.-Y., Yue, J., Wang, J. C., & Chien, S.-H. (2016). Coherent seasonal, annual, and quasi-biennial variations in ionospheric tidal/SPW amplitudes. *Journal of Geophysical Research: Space Physics, 121.* http://dx.doi.org/10.1002/2015JA022249

Cravens, T.E. & Killeen, T. L. (1988). Longitudinally asymmetric transport of Nitric Oxide in the E-region. *Planetary and Space Sciences*, 36(1), 11-19. http://dx.doi.org/10.1016/0032-0633(88)90142-0

Cravens, T. E., & Stewart, A. I. (1978). Global morphology of nitric oxide in the lower E region. *Journal of Geophysical Research*, 83(A6), 2446–2452. http://dx.doi.org/10.1029/JA083iA06p02446

Dalgarno, A. (1963). Vibrationally excited molecules in atmospheric reactions. *Planetary and Space Sciences*, 10, 19-28.

Demars, H. G. & Schunk, R. W. (2007). Thermospheric response to ion heating in the dayside cusp. *Journal of Atmospheric and Solar-Terrestrial Physics*, 69, 649–660, 2007. https://doi.org/10.1016/j.jastp.2006.11.002

Flynn, S. (2016-2017). Notes taken at various meetings and email conversations with Delores Knipp, Tomoko Matsuo, Martin Mlynczak, Linda Hunt, Liam Kilcommons, and Stan Solomon. Boulder, CO.

Fuller-Rowell, T. J. (1998). The ‘‘thermospheric spoon’’: A mechanism for the semiannual density variation. *Journal of Geophysical Research: Space Physics*, 103, 3951– 3956. http://dx.doi.org/10.1029/97JA03335

Gurman, J. B. (2017). *Solar Proton Events Affecting the Earth Environment*. NOAA Space Weather Prediction Center. https://umbra.nascom.nasa.gov/SEP/. Accessed September 23 2017.

Hartmann, D. L. (2016). Matrix Methods for Analysis of Structure in Data Sets. In *ATM 552 Notes: Matrix Methods: EOF, SVD, Etc.* (pp. 68-110).

Hedin, A. E., Salah, J.E., Evans, J.V., Reber, C. A., Newton, G. P., Spencer, N. W., … McClure, J. P. (1977). A global thermospheric model based on mass spectrometer and incoherent scatter data, MSIS 1, N2 density and temperature. *Journal of Geophysical Research*, 82(16), 2139–2147. http://dx.doi.org/10.1029/JA082i016p02139

Jacchia, L. G. & Slowey, J. (1963). Atmospheric heating in auroral zones: A Preliminary Analysis of the Atmospheric Drag of Injun III Satellite. Smithsonian Astrophysical Observatory, Special Report No. 136, NASA CR-52456, Cambridge, MA.

Jackman, C. H., Roble, R. G., & Fleming, E. L. (2007). Mesospheric dynamical changes induced by the solar proton events in October–November 2003. *Geophysical Research Letters*, 34, L04812. http://dx.doi.org/10.1029/2006GL028328

James, G., Witten, D., Hastie, T., & Tibshirani, R. (2015). *An Introduction to Statistical Learning*. New York, NY: Springer Science+Business Media New York.

Jones, M. Jr., Forbes, J.M, & Hagan, M. E. (2016). Solar cycle variability in mean thermospheric composition and temperature induced by atmospheric tides. *Journal of Geophysical Research: Space Physics*, 121, 5837–5855. http://dx.doi.org/10.1002/2016JA022701

Jones, M., Jr., Forbes, J. M., Hagan, M. E., & Maute, A. (2014). Impacts of vertically propagating tides on the mean state of the ionosphere-thermosphere system. *Journal of Geophysical Research: Space Physics*, 119(3), 2197–2213. http://dx.doi.org/10.1002/2013JA019744

Knipp, D., Kilcommons, L., Hunt, L., Mlynczak, M., Pilipenko, V., Bowman, B., … Drake, K. *(*2013*).* Thermospheric damping response to sheath-enhanced geospace storms. *Geophysical Research Letters,* 40*,* 1263–1267. http://dx.doi.org/10.1002/grl.50197

Knipp, D. J., Pette, D. V., Kilcommons, L. M., Isaacs, T. L., Cruz, A. A., Mlynczak, M. G., … Lin, C. Y. (2017). Thermospheric nitric oxide response to shock-led storms. *Space Weather, 15(2), 325-342*. http://dx.doi.org/10.1002/2016SW001567

Kockarts, G. (1980). Nitric oxide cooling in the terrestrial thermosphere. *Geophysical Research Letters*, 7(2), 137–140. http://dx.doi.org/10.1029/GL007i002p00137

Lei, J., Burns, A. G., Thayer, J. P., Wang, W., Mlynczak, M. G., Hunt, L. A., … Sutton, E. (2012). Overcooling in the upper thermosphere during the recovery phase of the 2003 October storms. *Journal of Geophysical Research*, 117, A03314. http://dx.doi.org/10.1029/2011JA016994

Lei, J., Thayer, J. P., Lu, G., Burns, A. G., Wang, W., Sutton, E. K., & Emery, B. A. (2011). Rapid recovery of thermosphere density during the October 2003 geomagnetic storms. *Journal of Geophysical Research*, 116, A03306. http://dx.doi.org/10.1029/2010JA016164

Liu H., Lühr, H., Henize, V., & Köhler, W. (2005). Global distribution of the thermospheric total mass density derived from CHAMP. *Journal of Geophysical Research*, 110, A04301. http://dx.doi.org/10.1029/2004JA010741

Liu, H., Lühr, H., & Watanabe, S. (2007). Climatology of the equatorial thermospheric mass density anomaly. *Journal of Geophysical Research*, 112, A05305. http://dx.doi.org/10.1029/2006JA012199

Liu, H., Lühr, H., & Watanabe, S. (2009). A solar terminator wave in thermospheric wind and density simultaneously observed by CHAMP. *Geophysical Research Letters*, 36, L10109. http://dx.doi.org/10.1029/2009GL038165

Liu, H., Thayer, J., Zhang, Y., & Lee, W. K. (2017). The non–storm time corrugated upper thermosphere: What is beyond MSIS?. *Space Weather*, 15, 746–760. http://dx.doi.org/10.1002/2017SW001618

Liu, H., Yamamoto, M., & Lühr, H. (2009). Wave-4 pattern of the equatorial mass density anomaly: A thermospheric signature of tropical deep convection. *Geophysical Research Letters*, 36, L18104. http://dx.doi.org/10.1029/2009GL039865

Lu, G., Mlynczak, M. G., Hunt, L. A., Woods, T. N., & Roble, R. G. (2010). On the relationship of Joule heating and nitric oxide radiative cooling in the thermosphere. *Journal of Geophysical Research*, 115, A05306. http://dx.doi.org/10.1029/2009JA014662

Luan, X., Wang, W., Burns, A., & Dou, X. (2016). Universal time variations of the auroral hemispheric power and their interhemispheric asymmetry from TIMED/GUVI observations. *Journal of Geophysical Research: Space Physics*, 121, 10,258–10,268. http://dx.doi.org/10.1002/2016JA022730

Maeda, S., Fuller-Rowell, T. J., & Evans, D. S. (1989). Zonally averaged dynamical and compositional response of the thermosphere to auroral activity during September 18–24, 1984. *Journal of Geophysical Research*, 94(A12), 16,869–16,883. http://dx.doi.org/10.1029/JA094iA12p16869

Maeda, S., Fuller-Rowell, T., & Evans, D. (1992). Heat budget of the thermosphere and temperature variations during the recovery phase of a geomagnetic storm. *Journal of Geophysical Research*, 97(A10), 14,947–14,957. http://dx.doi.org/10.1029/92JA01368

Marsh, D. R., & Russell, J. M. (2000). A tidal explanation for the sunrise/sunset anomaly in HALOE low-latitude nitric oxide observations. *Geophysical Research Letters*, 27(19), 3197-3200. http://dx.doi.org/10.1029/2000GL000070

Marsh, D. R., Solomon, S. C., & Reynolds, A. E. (2004). Empirical model of nitric oxide in the lower thermosphere. *Journal of Geophysical Research, 109*(A07301). http://dx.doi.org/10.1029/2003JA010199

Matsuo, T. & Forbes, J. (2010). Principal modes of thermospheric density variability: Empirical orthogonal function analysis of CHAMP 2001–2008 data. *Journal of Geophysical Research, 115(*A07309). http://dx.doi.org/10.1029/2009JA015109

Matsuo, T., Richmond, A. D., & Lu, G. (2005). Optimal Interpolation analysis of high-latitude ionospheric electrodynamics using empirical orthogonal functions: Estimation of dominant modes of variability and temporal scales of large-scale electric fields. *Journal of Geophysical Research*, 110(A06301). http://dx.doi.org/10.1029/2004JA010531

Matsuo, T., Richmond A. D., & Nychka, D. W. (2002). Modes of high-latitude electric field variability derived from DE-2 measurements: Empirical Orthogonal Function (EOF) analysis. *Geophysical Research Letters*, 29(7), 1107. http://dx.doi.org/0.1029/2001GL014077

McGranaghan, R., Knipp, D. J., McPherron, R. L., & Hunt, L. A. (2014). Impact of equinoctial high-speed stream structures on thermospheric responses. *Space Weather*, 12, 277–297. http://dx.doi.org/10.1002/2014SW001045

McGuire, R. (2017). MSIS-E-90 Atmosphere Model. NASA/Goddard Space Flight Center, Greenbelt, MD. https://omniweb.gsfc.nasa.gov/vitmo/msis_vitmo.html. Accessed October 4, 2017.

McGuire, R. (2017). *OMNIWeb*. Space Physics Data Facility, NASA/Goddard Space Flight Center, Greenbelt, MD. https://omniweb.gsfc.nasa.gov/form/dx1.html. Accessed April 19 2017.

Mendillo, M., Rishbeth, H., Roble, R. G., & Wroten, J. (2002). Modelling F2-layer seasonal trends and day-to-day variability driven by coupling with the lower atmosphere. *Journal of Atmospheric and Solar-Terrestrial Physics*, 64, 1911 –1931. http://dx.doi.org/10.1016/S1364-6826(02)00193-1

Miyoshi, Y., Fujiwara, H., Forbes, J. M., & Bruinsma, S. L. (2009). Solar terminator wave and its relation to the atmospheric tide. *Journal of Geophysical Research*, 114, A07303, http://dx.doi.org/10.1029/2009JA014110

Mlynczak, M. & Hunt, L. (2015). SABER NO Point Flux text data files. SABER Data Version 2.0. https://saber.gats-inc.com.

Mlynczak, M., Martin-Torres, F. J., Crowley, G., Kratz, D. P., Funke, B., Lu, G., … Paxton, L. (2005). Energy transport in the thermosphere during the solar storms of April 2002. *Journal of Geophysical Research,* 110(A12S25). http://dx.doi.org/10.1029/2005JA011141

Mlynczak, M. G., Martin-Torres, F. J., Mertens, C. J., Marshall, B. T., Thompson, R. E., Kozyra, J. U., … Woods, T. (2008). Solar-terrestrial coupling evidenced by periodic behavior in geomagnetic indexes and the infrared energy budget of the thermosphere. *Geophysical Research Letters,* 35, L05808. http://dx.doi.org/10.1029/2007GL032620

Mlynczak, M., Martin-Torres, F. J., Russell, J., Beaumont, K., Jacobson, S., Kozyra, J., … Paxton, L. (2003). The natural thermostat of nitric oxide emission at 5.3 μm in the thermosphere observed during the solar storms of April 2002. *Geophysical Research Letters,* 30(21), 2100. http://dx.doi.org/10.1029/2003GL017693.

Mukhtarov, P. & Pancheva, D. (2011). Global ionospheric response to nonmigrating DE3 and DE2 tides forced from below. *Journal of Geophysical Research*, 116, A05323. http://dx.doi.org/ 10.1029/2010JA016099

NOAA (2002-2015). *Daily Solar, Particle, and Geomagnetic Data*. NOAA Space Weather Prediction Center. ftp://ftp.swpc.noaa.gov/pub/indices/old_indices/. Accessed March 1, 2017.

North, G. R., Bell, T. L., & Cahalan, R. F. (1982). Sampling Errors in the Estimation of Empirical Orthogonal Functions. *American Meteorological Society*, 110, 699-706. https://doi.org/10.1175/1520-0493(1982)110<0699:SEITEO>2.0.CO;2

Oberheide, J., & Forbes, J. M. (2008). Thermospheric nitric oxide variability induced by nonmigrating tides. *Geophysical Research Letters*, 35, L16814. http://dx.doi.org/10.1029/2008GL034825

Oberheide, J., Forbes, J. M., Häusler, K., Wu, Q., & Bruinsma, S. L. (2009). Tropospheric tides from 80–400 km: Propagation, interannual variability, and solar cycle effects. *Journal of Geophysical Research*, 114, D00I0. http://dx.doi.org/10.1029/2009JD012388

Oberheide, J., Mlynczak, M. G., Mosso, C. N., Schroeder, B. M., Funke, B., & Maute, A. (2013). Impact of tropospheric tides on the nitric oxide 5.3 um infrared cooling of the low-latitude thermosphere during solar minimum conditions. *Journal of Geophysical Research: Space Physics, 118,* 7283-7293. http://dx.doi.org/10.1002/2013JA019278

Observatori de l'Ebre (2013). List of sudden commencements. Ramon Llull University (URL): Observatori de l'Ebre. http://www.obsebre.es/en/institution. Accessed September 20, 2017.

Ogawa, T. (1976). Excitation processes of infrared atmospheric emissions. *Planetary and Space Sciences*, 24, 749-756. http://dx.doi.org/10.1016/0032-0633(76)90111-2

Paetzold, H. K., & Zschörner, H. (1961). An annual and a semiannual variation of the upper air density. *Pure and Applied Geophysics*, 48, 85– 92.

Pancheva, D., & Mukhtarov, P. (2010). Strong evidence for the tidal control on the longitudinal structure of the ionospheric F region. *Geophysical Research Letters*, 37, L14105. http://dx.doi.org/10.1029/2010GL044039

Picone, J. M., Hedin, A. E., Drob, D. P., & Aikin, C. C. (2002). NRLMSISE-00 empirical model of the atmosphere: Statistical comparisons and scientific issues. *Journal of Geophysical Research*, 107(A12), 1468. http://dx.doi.org/10.1029/2002JA009430

Qian, L., Solomon, S. C., & Kane, T. J. (2009). Seasonal variation of thermospheric density and composition. *Journal of Geophysical Research*, 114, A01312. http://dx.doi.org/10.1029/2008JA013643

Rentz, S. & Lühr, H. (2008). Climatology of the cusp-related thermospheric mass density anomaly, as derived from CHAMP observations. *Annales Geophysicae*, 26, 2807-2823. https://doi.org/10.5194/angeo-26-2807-2008

Richards, P. G. (2004). On the increases in nitric oxide density at midlatitudes during ionospheric storms. *Journal of Geophysical Research,* 109, A06304. https://doi.org/10.1029/2003JA010110

Ridley, A. J., Crowley, G., Link, R., Frahm, R., Winningham, J. D., Sharber, J. R., & Russell, J. (1999). Variations of the thermospheric nitric oxide mass mixing ratio as a function of Kp, altitude, and magnetic local time. *Geophysical Research Letters, 26*(11), 1541-1544. https://doi.org/10.1029/1999GL900301

Rusch, D. W., Gerard, J.-C., & Fesen, C. G. (1991). The Diurnal Variation of NO, N(2D), and Ions in the Thermosphere: A Comparison of Satellite Measurements to a Model. *Journal of Geophysical Research*, 96(A7), 11,331-11,339.

Sinnhuber, M., Nieder, H., & Wieteres, N. (2012). Energetic Particle Precipitation and the Chemistry of the Mesosphere/Lower Thermosphere. *Surveys in Geophysics,* 33, 1281–1334. http://dx.doi.org/10.1007/s10712-012-9201-3

Solomon, S. C., Barth, C. A., & Bailey, S. M. (1999). Auroral production of nitric oxide measured by the SNOE satellite. *Geophysical Research Letters*, 26, 1259–1262. http://dx.doi.org/10.1029/1999GL900235

Solomon, S. C., Burns, A. G., Emery, B. A., Mlynczak, M. G., Qian, L., Wang, W., … Wiltberger, M. (2012). Modeling studies of the impact of high-speed streams and co-rotating interaction regions on the thermosphere-ionosphere. *Journal of Geophysical Research*, 117, A00L11. http://dx.doi.org/10.1029/2011JA017417

SORCE: Solar Radiation and Climate Experiment. (2017). Available Data Access. http://lasp.colorado.edu/home/sorce/data/#avail_data. Accessed March 25, 2017.

Strobel, D. F. (1971). Diurnal Variation of Nitric Oxide in the Upper Atmosphere. *Journal of Geophysical Research*, 76(10), 2441-2452.

Trifonov, A. N., Makarov, N. A. Merzlyakov, E. G. (2016). Effects of Solar Proton Events in the Mesosphere/Lower Thermosphere Region According to the Data of Meteo Radar Wind Measurements at High and Middle Latitudes. *Geomagnetism and Aeronomy*, 56(2), 163-177. http://dx.doi.org/10.1134/S0016793216010126

Valtonen, E., Laitinen, T., & Huttunen-Heikinmaa, K. (2005). Energetic particle signatures of geoeffective coronal mass ejections. *Advances in Space Research*, 36, 2295-2302.

Van der Meeren, C. & Laundal, K. M. (2016). *AACGM-v2 Python Library.* Version 2.0.0. http://aacgmv2.readthedocs.io/en/stable/index.html. Accessed February 12, 2017.

Venkataramani, K., Yonker, J. D., & Bailey, S. M. (2016). Contribution of chemical processes to infrared emissions from nitric oxide in the thermosphere. *Journal of Geophysical Research Space Physics,* 121, 2450–2461. http://dx.doi.org/10.1002/2015JA022055

Walterscheid, R. L. (1982). The semiannual oscillation in the thermosphere as a conduction mode. *Journal of Geophysical Research*, 87, 10,527– 10,535. http://dx.doi.org/10.1029/JA087iA12p10527

Wang, Y. (2006). List of Interplanetary Coronal Mass Ejections (ICMEs). University of Science and Technology of China: Space Physics Division. http://space.ustc.edu.cn/dreams/wind_icmes/. Accessed September 28, 2017.

Weimer, D. R., Mlynczak, M. G., Hunt, L. A., & Tobiska, W. K. (2015). High correlations between temperature and nitric oxide in the thermosphere. *Journal of Geophysical Research: Space Physics, 120*, 5998–6009. http://dx.doi.org/10.1002/2015JA021461

Weisstein, E. W. Associated Legendre Polynomial. MathWorld: A Wolfram Web Resource. http://mathworld.wolfram.com/AssociatedLegendrePolynomial.html. Accessed April 30, 2017.

Weisstein, E. W. Spherical Harmonic. MathWorld: A Wolfram Web Resource. http://mathworld.wolfram.com/SphericalHarmonic.html. Accessed April 30, 2017.

Wissing, J. M., & Kallenrode, M.-B. (2009). Atmospheric Ionization Module Osnabrück (AIMOS): A 3-D model to determine atmospheric ionization by energetic charged particles from different populations. *Journal of Geophysical Research*, 114, A06104. http://dx.doi.org/10.1029/2008JA013884

Woodraska, D. L. & Woods, T. N. (2012). TIMED SEE Version 11 Data Products. University of Colorado, Boulder: Laboratory for Atmospheric and Space Physics. http://lasp.colorado.edu/home/see/data. Obtained October 4, 2017.

Yee, J., E. R. Talaat, A. B. Christensen, T. L. Killeen, J. M. Russell III, T. N. Woods. (2003). TIMED Instruments. *Johns Hopkins APL Technical Digest,* 24(2).

Zheng, Y. & Evans, R. (2014). *Solar Energetic Particles (SEPs).* SW REDI Boot Camp.

Appendix A

Mathematical Definition of Spherical Harmonics

For colatitude $\theta = [0, \pi]$ (from the north geomagnetic pole to the south geomagnetic pole) and longitude $\varphi = [0, 2\pi]$ (or 00:00 to 24:00 MLT), the spherical harmonics are defined as:

$$for\ degree\ l = 0 \ldots 7\ and\ order\ m, -l \leq m \leq l,$$

$$Y_l^m(\theta, \varphi) = \sqrt{\frac{2l+1}{4\pi}\frac{(l-m)!}{(l+m)!}} P_l^m \cos(\theta) \cos(m\varphi), where$$

$$P_l^m(x) = \frac{(-1)^m}{2^l l!}(1-x^2)^{\frac{m}{2}}\frac{d^{l+m}}{dx^{l+m}}(x^2-1)^l, m > 0$$

$$P_l^{-m}(x) = (-1)^m \frac{(1-m)!}{(1+m)!} P_l^m(x), m < 0$$

(Obtained from Weisstein)

Obtaining EOFs using a Sequential Nonlinear Regression Algorithm

While EOFs are conventionally obtained through eigen analysis of the covariance of a gridded set of non-sparse observations, the SABER NOF data set is nonuniform and too large to use this method. Instead, the sequential nonlinear regression analysis explained by Matsuo et al. (2002) is used to obtain the EOFs in this work, which is summarized here.

1. **Determine an orthogonal basis**

   For this study, the first 64 real spherical harmonics (up to degree 7) are used as a basis set (see above for their mathematical definition). Let Φ be the spherical harmonic matrix of size $L \times 64$, where L is the number of data points in the SABER NOF data set (over 7

million). Each NOF value in the SABER NOF data set has a corresponding colatitude, longitude, and time, which are not evenly distributed in space or time.

2. Compute the mean field

Least-squares linear regression is used to determine a set of coefficients, vector $\beta^{(0)}$ of size 64, by solving the equation:

$$y = \Phi\beta^{(0)}$$

Where y is the SABER NOF data vector of length L. The mean spatial NOF field in terms of spherical harmonics is a vector of size L given by $\Phi\beta^{(0)}$. The residual can then be calculated:

$$y' = y - \Phi\beta^{(0)}$$

3. Compute the first estimate of EOF 1

Least-squares linear regression is used to compute $\beta^{(1)}$ by solving the equation:

$$y' = \Phi\beta^{(1)}$$

$\beta^{(1)}$ is then normalized. The first EOF is initially given by $\Phi\beta^{(1)}$.

4. Iteratively determine the EOF 1 coefficients and amplitude

For each point along the satellite track (or orbit number) j, compute the scalar $\alpha_1'(j)$ by performing least-squares linear regression on the equation:

$$y'(j) = \alpha_1'(j)\Phi(j)\beta^{(1)}$$

Compute this for all J orbits to obtain the vector α_1' of size J. Interpolate this vector to obtain the EOF 1 vector amplitudes α_1 of size L (there is one value of α_1 for all points along the same satellite track).

Determine the cost function (which represents the difference between the data residual and the EOF 1 model):

$$s^{(1)} = sum((y' - \alpha_1 \Phi \beta^{(1)})^2)$$

Minimize this by re-computing $\beta^{(1)}$ by performing least-squares linear regression on the equation:

$$y' = \alpha_1 \Phi \beta^{(1)}$$

$\beta^{(1)}$ is normalized once more. In this analysis, step 4 is repeated 20 times to iteratively and alternatively determine $\beta^{(1)}$ and α_1 by minimizing the cost function each time. Each iteration leads to a more accurate fit.

Once a sufficient fit is determined, the first EOF is given by $\Phi\beta^{(1)}$, and its amplitude in time is given by α_1.

5. Compute EOF 2, …, n and their amplitudes

Subtract the EOF 1 fit from y':

$$y' = y' - \alpha_1 \Phi \beta^{(1)}$$

Now y' represents the residual with the mean and the first mode of variability subtracted. Perform QR decomposition (i.e., the Gram-Schmidt method) to determine an orthogonal basis Φ' to $\beta^{(1)}$. Determine $\beta^{(2)}$ from least-squares nonlinear regression of the equation:

$$y' = \Phi'\beta^{(2)}$$

Normalize and rotate $\beta^{(2)}$ back into the original basis (colatitude and longitude). $\beta^{(2)}$ is orthogonal to $\beta^{(1)}$.

Perform step 4 to iteratively and alternatively determine $\beta^{(2)}$and α_2 by minimizing the new cost function. Once these are adequately determined, subtract EOF 2 and its amplitude from the residual:

$$y' = y' - \alpha_2\Phi\beta^{(2)}$$

Perform step 4 for each $\beta^{(n)}$and α_n, subtracting each EOF fit from the residual (each with a lower cost, or model error) each time. This method ensures that each EOF n is orthogonal to the previous $n - 1$ EOFs.

6. Describe the EOF Model

The final EOF model, which describes the SABER NOF data set, can be defined as a summation of the spatial mean and the first n spatial EOFs and their temporal amplitudes:

$$y \approx \Phi\beta^{(0)} + \alpha_1\Phi\beta^{(1)} + \ldots + \alpha_1\Phi\beta^{(n)}$$

In the analysis presented here, the SABER NOF data set is modeled using the mean and the first $n = 4$ EOFs, which describes 83% of the total variance in the data set (as determined by the final cost function of the model).

Appendix B

EOFs as seen from the North and South Geomagnetic Poles

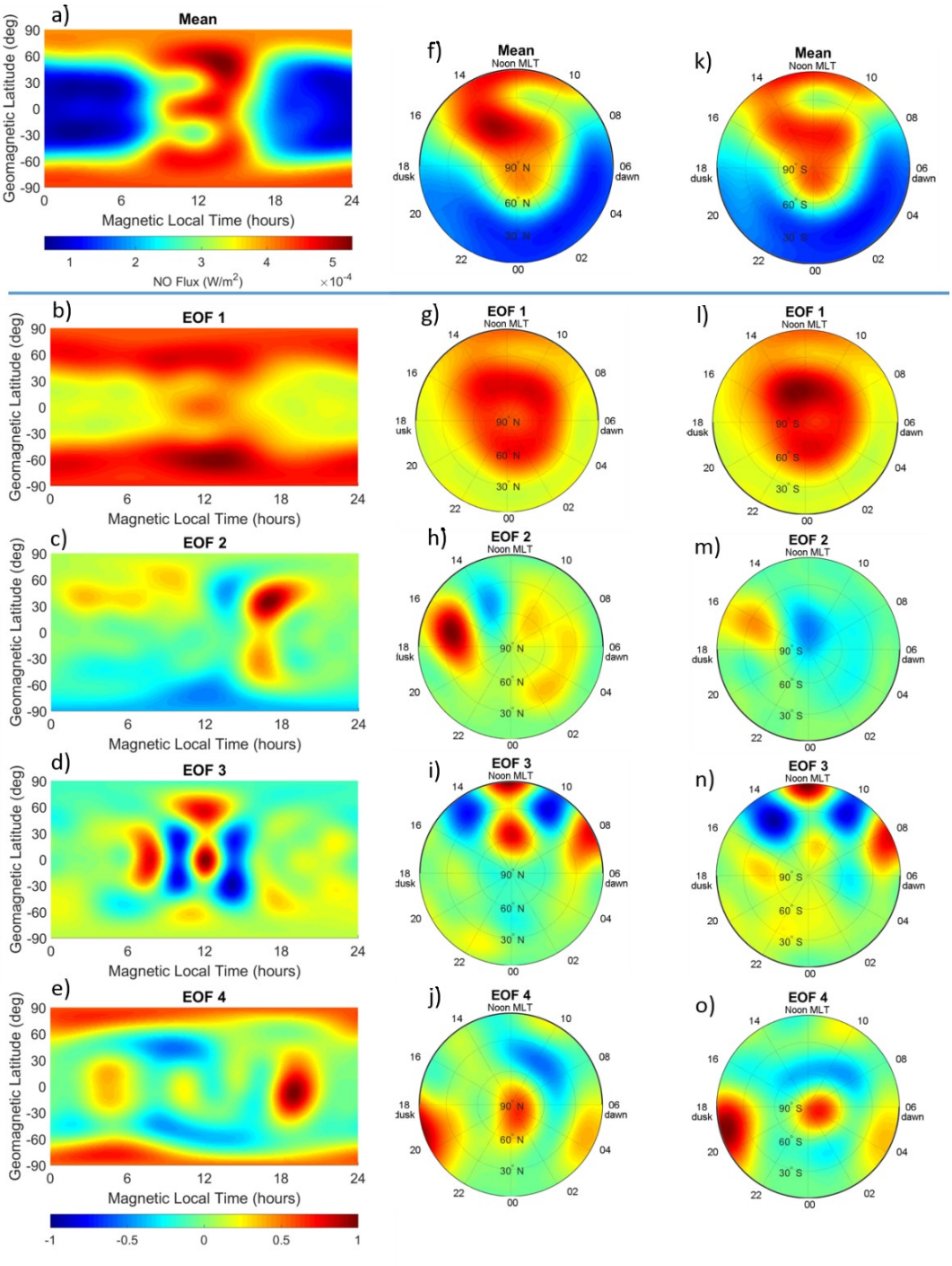

Figure A1. a) The mean NO flux in geomagnetic coordinates (Same as Figure 2). b-e) The EOFs (NO flux variability) (Same as those in Figure 3). Figures f-j show the same maps as seen from the North Geomagnetic Pole, and figures k-o show the same maps as seen from the South Geomagnetic Pole.

Appendix C

EOF Model Performance

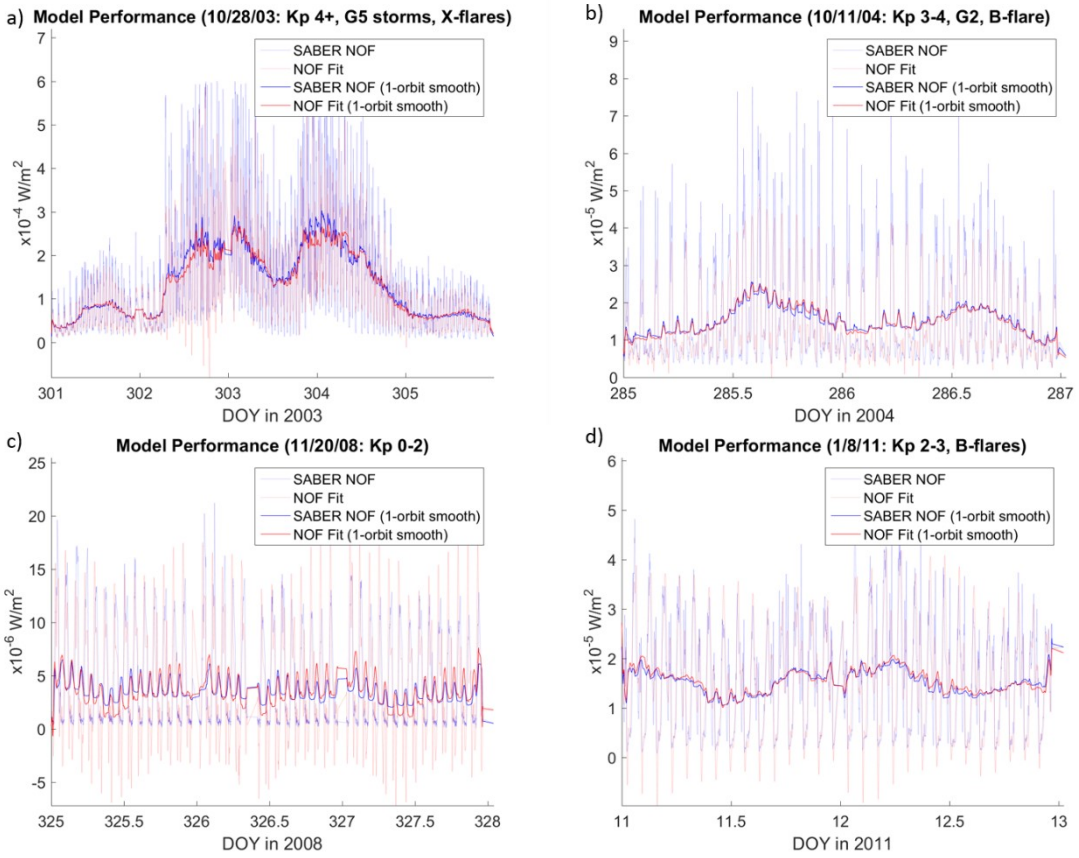

Figure A2. NO Flux model performance for the mean + EOFs 1 through 5, representing 85% of the total covariance in the original SABER NO Flux data set. All figures show the original SABER NO flux along the satellite path sampled approximately every minute (light blue) and the same data smoothed over 1 orbit (blue), and the model fit along the same path (light red) and the same data smoothed over 1 orbit (red). A) shows the performance near solar maximum during intense storm times. B) shows the performance near solar maximum during moderate storm times. C) shows the performance near solar minimum during very quiet times. Figure D) shows the performance in-between solar minimum and solar maximum during moderate storm times.

Captions for Supplementary Movies of Model Performance

Movie S1. ms01.avi: A video of the mean NOF + EOF 1 + EOF 3 in W/m^2 for the double CME/SEP event of late October 2003. 60 MeV+ Proton flux (pfu) and EOF amplitudes (unitless) are also shown.

Movie S2. ms02.avi: A video of the mean NOF + EOF 1 + EOF 4 in W/m^2 for the double CME & geomagnetic storm events of late October 2003. 24-hour smoothed Kp and EOF amplitudes (unitless) are also shown.

Movie S3. ms03.avi: A video of the mean NOF + EOF 1 + EOF 4 in W/m^2 for the double CME events of 11/10/2004. 24-hour smoothed Kp and EOF amplitudes (unitless) are also shown.

Movie S4. ms04.avi: A video of the mean NOF + EOF 1 + EOF 4 in W/m^2 for the single CME & SEP events on 5/15/2005. 24-hour smoothed Kp and EOF amplitudes (unitless) are also shown.

Movie S5. ms05.avi: A video of the mean NOF + EOF 1 + EOF 4 in W/m^2 for the single CME & SEP events on 6/25/2015. 24-hour smoothed Kp and EOF amplitudes (unitless) are also shown.

Movie S6. ms06.avi: A video of SABER's NOF in W/m^2 from 1/25/2002 to 10/23/2015 in geomagnetic coordinates along the satellite sampling path. Since the solar sampling time of SABER is ~60 days, the data has been smoothed over a 60-day period. To better show NOF variability, $\log_{10}$(NOF) is shown.

Movie S7. ms07.avi: A video of the EOF model (using the first 5 EOFs, representing 85% of the total covariance of the dataset) of SABER's NOF in W/m^2 from 1/25/2002 to 10/23/2015 in geomagnetic coordinates along the satellite sampling path. Since the solar sampling time of SABER is ~60 days, the data has been smoothed over a 60-day period. To better show NOF variability, $\log_{10}$(NOF) is shown.

Movie S8. ms08.avi: A video of SABER's NOF in W/m^2 from 1/25/2002 to 10/23/2015 in geomagnetic coordinates using a rectangular grid. Since the solar sampling time of SABER is ~60 days, the data has been smoothed over a 60-day period. To better show NOF variability, $\log_{10}$(NOF) is shown.